



Contents lists available at SciVerse ScienceDirect

Journal of the Mechanics and Physics of Solids

journal homepage: www.elsevier.com/locate/jmps

Computational optogenetics: A novel continuum framework for the photoelectrochemistry of living systems

Jonathan Wong^a, Oscar J. Abilez^b, Ellen Kuhl^{a,b,c,*}^a Department of Mechanical Engineering, Stanford University, Stanford, CA 94305, USA^b Department of Bioengineering, Stanford University, Stanford, CA 94305, USA^c Department Cardiothoracic Surgery, Stanford University, Stanford, CA 94305, USA

ARTICLE INFO

Article history:

Received 20 August 2011

Received in revised form

21 December 2011

Accepted 7 February 2012

Available online 11 February 2012

Keywords:

Optogenetics

Photoelectrochemistry

Biophysics

Continuum mechanics

Finite element method

ABSTRACT

Electrical stimulation is currently the gold standard treatment for heart rhythm disorders. However, electrical pacing is associated with technical limitations and unavoidable potential complications. Recent developments now enable the stimulation of mammalian cells with light using a novel technology known as optogenetics. The optical stimulation of genetically engineered cells has significantly changed our understanding of electrically excitable tissues, paving the way towards controlling heart rhythm disorders by means of photostimulation. Controlling these disorders, in turn, restores coordinated force generation to avoid sudden cardiac death. Here, we report a novel continuum framework for the photoelectrochemistry of living systems that allows us to decipher the mechanisms by which this technology regulates the electrical and mechanical function of the heart. Using a modular multiscale approach, we introduce a non-selective cation channel, channelrhodopsin-2, into a conventional cardiac muscle cell model via an additional photocurrent governed by a light-sensitive gating variable. Upon optical stimulation, this channel opens and allows sodium ions to enter the cell, inducing electrical activation. In side-by-side comparisons with conventional heart muscle cells, we show that photostimulation directly increases the sodium concentration, which indirectly decreases the potassium concentration in the cell, while all other characteristics of the cell remain virtually unchanged. We integrate our model cells into a continuum model for excitable tissue using a nonlinear parabolic second-order partial differential equation, which we discretize in time using finite differences and in space using finite elements. To illustrate the potential of this computational model, we virtually inject our photosensitive cells into different locations of a human heart, and explore its activation sequences upon photostimulation. Our computational optogenetics tool box allows us to virtually probe landscapes of process parameters, and to identify optimal photostimulation sequences with the goal to pace human hearts with light and, ultimately, to restore mechanical function.

© 2012 Elsevier Ltd. All rights reserved.

* Corresponding author at: Department of Mechanical Engineering, Stanford University, Stanford, CA 94305, USA. Tel.: +1 650 450 0855; fax: +1 650 725 1587.

E-mail addresses: jonjwong@stanford.edu (J. Wong), ojabilez@stanford.edu (O.J. Abilez), ekuhl@stanford.edu (E. Kuhl).

URL: <http://biomechanics.stanford.edu> (E. Kuhl).

1. Motivation

The human heart propels over 7000 l of blood through the body daily, beating more than 40 million times a year. It is a remarkably efficient, durable, and reliable mechanical pump, precisely regulated by spatially and temporally varying electrical and chemical fields. Disturbed conduction and uncoordinated electrical signals can induce abnormal heart rhythms, which may critically reduce mechanical function (Dubin, 2000; Tsamis et al., 2011). A delicate balance between the electrical and chemical gradients across the cell membrane governs the electrophysiological activity of excitable cardiac cells. To maintain these gradients, the cell membrane is selectively permeable with respect to different ions at different points in time (Berne and Levy, 2001). In a cardiac muscle cell, for example, the potential difference across the cell membrane is approximately -80 mV at rest, meaning the cell is negatively charged. It can be excited by an external electrical stimulus that pushes its transmembrane potential beyond a critical threshold value. This triggers the influx of sodium ions, generating a rapid depolarization, and the transmembrane potential increases to $+20$ mV. Over time, the coordinated interplay between sodium, potassium, and calcium ions brings the transmembrane potential smoothly back to its resting state (Keener and Sneyd, 2004). Since the late 1950s, permanent cardiac pacemakers have been used successfully to correct rhythm disorders and restore smoothly propagating waves of electrical excitation (Furman and Schwedel, 1959). Pacemakers deliver electrical stimuli via implanted pacing leads that are in contact with the heart muscle. Although permanent pacemaker implantation is a standard procedure today, pacing lead placement continues to be a subject of great controversy (Modi et al., 2011). Choosing the optimal pacing site is becoming more challenging (Puwal and Roth, 2009), in particular in view of novel stimulation strategies such as single chamber, dual chamber, and biventricular pacing. A potential complication of lead placement is cardiac perforation, which can have severe clinical consequences including pericardial effusion, cardiac tamponade, pneumothorax, and death (Mahapatra et al., 2005). However, to date, there is no conceptual alternative to electrical pacing that avoids direct contact stimulus delivery (Khan et al., 2005).

For more than 40 years, biologists have studied microorganisms that produce proteins to directly regulate the flow of charged ions across their plasma membrane in response to light (Oesterhelt and Stoeckenius, 1971). The first identified protein of this kind was the light-gated ion pump bacteriorhodopsin, transporting positively charged hydrogen ions across the cell membrane (Oesterhelt and Stoeckenius, 1971). While bacteriorhodopsin naturally acts as an on-switch for electrically active cells, the second reported light-gated ion pump, halorhodopsin, transports negatively charged chloride ions, thereby acting as an off-switch (Matsuno-Yagi and Mukohata, 1977). Despite intense research (Vsedolodov, 1998), the first reported light-gated ionic channel, channelrhodopsin, was only identified 10 years ago (Nagel et al., 2002), but has since then revolutionized neuroscience. Channelrhodopsin consists of seven transmembrane proteins embedded in the lipid bilayer (Feng and Klug, 2006) and absorbs blue light through its interaction with retinal, see Fig. 1. Since the early 1990s, we have known that phototaxis and photophobic responses in the green alga *Chlamydomonas reinhardtii* are mediated by rhodopsins with a microbial-type all-*trans* retinal chromophore (Hegemann et al., 1991). The photochemical isomerization of this all-*trans* retinal to 13-*cis* retinal is illustrated in Fig. 2. It occurs at peak absorption wavelengths of 470 nm, opening channelrhodopsin non-specifically to sodium, potassium, and calcium cations in response to blue light. In the dark, the covalently bound retinal spontaneously relaxes to all-*trans*, providing closure of the channel and regeneration of the chromophore. In 2005, channelrhodopsin was first introduced genetically using engineered viruses (Boyden et al., 2005), a technique that is now widely known as optogenetics (Deisseroth, 2011). Since then, optical tools to control the electrical activity of nerve cells have rapidly evolved (Szobota and Isacoff, 2010), and are now gaining widespread use in neuronal research and medicine (Hegemann and Möglich, 2011). While initial applications of optogenetics have been restricted exclusively to the neuronal system, optogenetic tools have now advanced to a level of maturity where they can

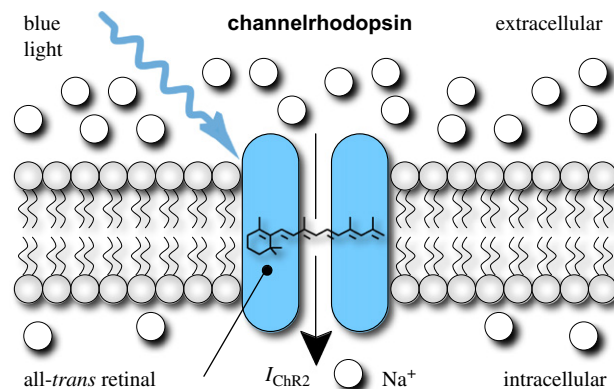


Fig. 1. Channelrhodopsin-2 is a light-gated cation channel native to the green alga *Chlamydomonas reinhardtii*. It consists of seven transmembrane proteins and absorbs blue light through its interaction with retinal. Photoisomerization of retinal opens the channel to sodium ions, which have a higher concentration outside than inside the cell. To make our cells responsive to light, and allow sodium concentrations to equilibrate, we induce channelrhodopsin into a conventional cardiac muscle cell model.

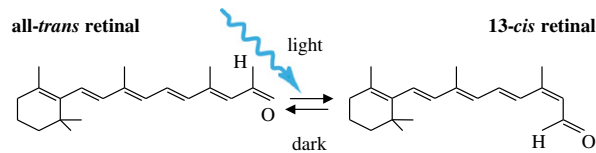


Fig. 2. Channelrhodopsin-2 is activated by photoisomerization of all-*trans* retinal to 13-*cis* retinal at wavelengths of 470 nm. After photoisomerization, the covalently bound retinal spontaneously relaxes to all-*trans* in the dark, providing closure of the ion channel and regeneration of the chromophore.

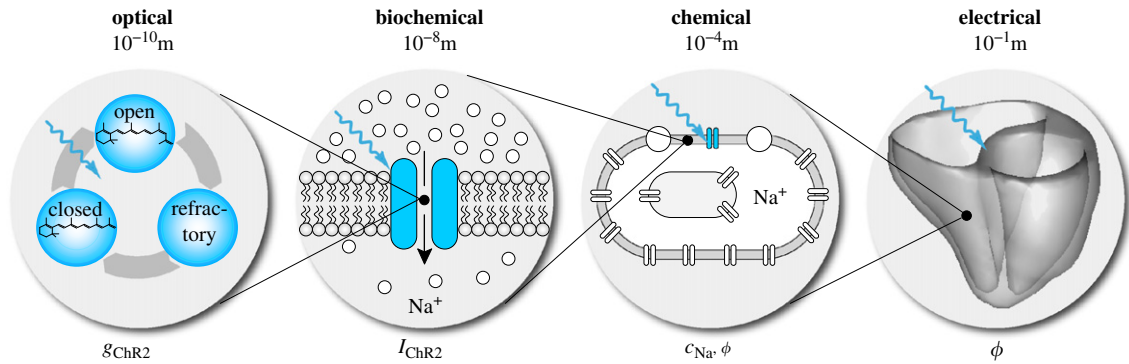


Fig. 3. Multiscale model for the photoelectrochemistry of living systems. Optical stimulation opens the cation channel channelrhodopsin g_{ChR2} . This initiates a photocurrent I_{ChR2} increasing the chemical concentration of sodium ions c_{Na} inside the cell. Concentration changes evoke changes in the electrical potential ϕ , which propagates across the tissue system in the form of smooth excitation waves.

confidently be applied to other cells and organs. Natural first candidates are stem cells, electrically active glial cells, muscle cells, and cardiac cells (Arrenberg et al., 2010; Jia et al., 2011). Since light can be delivered at a distance, optical pacing has the potential to become a more precise and less invasive alternative to existing electrical pacing strategies (Abilez et al., 2011).

The objective of this paper is to establish a novel continuum model for the photoelectrochemistry of living systems that will allow us to virtually explore the potential of optogenetic pacing. The rationale for creating such a model is that it will enable patient-specific predictions of ion channel dynamics, ionic concentrations, and action potential profiles across the heart, which are outside the reach of experimental measurements in humans. Fig. 3 illustrates the underlying approach in which the different physical fields interact across the different scales. On the molecular level, optical stimulation opens the cation channel channelrhodopsin initiating a photocurrent. On the subcellular level, this photocurrent increases the chemical concentration of sodium ions inside the cell. On the cellular level, concentration changes evoke changes in the electrical potential and excite the cell. On the tissue level, changes in the electrical potential propagate across the system in the form of smooth excitation waves.

In Section 2, we summarize the mathematical model for the channelrhodopsin photocycle and illustrate how channelrhodopsin can be introduced into a conventional cardiac cell model via an additional photocurrent governed by a light-sensitive gating variable. We characterize this additional photocurrent in Section 3, and demonstrate its impact on the intracellular ion concentrations in Section 4, and on the transmembrane potential in Section 5. In a side-by-side comparison with conventional cardiac muscle cells, we perform virtual case studies to demonstrate the features of genetically engineered light-sensitive cells in terms of gating variables, ionic currents, ion concentrations, and transmembrane potentials. Since our baseline model for conventional cardiac cells is well-characterized and fairly standard, we summarize its equations in the Appendix. We proceed by embedding these single cells into a novel continuum framework for photoelectrochemistry to simulate the spatial and temporal variation of electrical and chemical fields across the human heart. We briefly summarize the finite element discretization of the governing equations in Section 6. In Section 7, we virtually inject our light-sensitive cells into different locations of a human heart and explore its response to photostimulation. In Section 8, we conclude by discussing computational optogenetics and the potential of turning light into force in the context of pacing hearts with light.

2. Mathematical model of channelrhodopsin photocycle

To model the light sensitivity of channelrhodopsin, we adopt the kinetics of a three-state photocycle model (Hegemann et al., 2005; Nikolic et al., 2009), which consists of a closed, photosensitive, excitable state g_{closed} , an open state g_{ChR2} , and a closed, desensitized, absolutely refractory state g_{refrac} (Nagel et al., 2003), as illustrated in Fig. 4. Upon photoabsorption, molecules which are in the closed state g_{closed} undergo a fast transition into the open state g_{ChR2} . After being open for some time, molecules spontaneously transition into the absolutely refractory state g_{refrac} , where the ion channels are closed, but the molecules are not yet ready to photoswitch again. After the refractory period, the molecules finally return to the closed

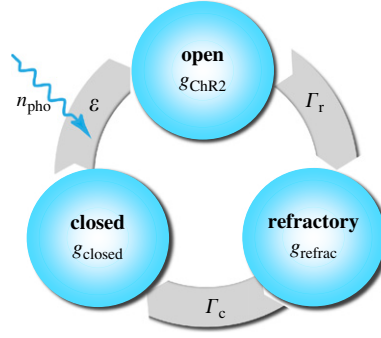


Fig. 4. Three-state model for the channelrhodopsin photocycle. Upon photo absorption, molecules in the closed state g_{closed} undergo a fast transition into the open state g_{ChR2} . The molecules spontaneously turn into the refractory state g_{refrac} where the ion channels are closed, but the molecules are not yet ready to photoswitch again. After the refractory period, the molecules return to the closed state g_{closed} , ready to undergo a new photocycle when subjected to light (Nagel et al., 2003; Nikolic et al., 2006).

state g_{closed} , ready to undergo a new photocycle when exposed to light (Nikolic et al., 2006). Fig. 4 suggests the following first-order model for the channelrhodopsin photocycle,

$$\begin{aligned} \dot{g}_{\text{ChR2}} &= \varepsilon n_{\text{pho}} g_{\text{closed}} - \Gamma_r g_{\text{ChR2}} \\ \dot{g}_{\text{refrac}} &= \Gamma_r g_{\text{ChR2}} - \Gamma_c g_{\text{refrac}} \\ \dot{g}_{\text{closed}} &= \Gamma_c g_{\text{refrac}} - \varepsilon n_{\text{pho}} g_{\text{closed}} \end{aligned} \quad (1)$$

where Γ_r and Γ_c are the rates of recovery and full closure, ε is the quantum efficiency of the channelrhodopsin system, and n_{pho} is the number of photons hitting the cell per second. Here, we choose $\Gamma_r = 0.06129$, $\Gamma_c = 0.00422$, and $\varepsilon n_{\text{pho}} = 0.018$. Herein, g_{ChR2} , g_{refrac} , and g_{closed} define the fraction of molecules in the open, refractory, and closed states. Initially, all molecules are in the closed state, i.e., $g_{\text{closed}} = 1$, $g_{\text{ChR2}} = 0$, and $g_{\text{refrac}} = 0$. Since all three fractions sum up to one, i.e., $g_{\text{ChR2}} + g_{\text{refrac}} + g_{\text{closed}} = 1$, the photocycle system (1) can be characterized through two independent variables (Ishizuka et al., 2006), e.g., the fraction of molecules in the open and in the refractory states:

$$\begin{aligned} \dot{g}_{\text{ChR2}} &= \varepsilon n_{\text{pho}} - [\varepsilon n_{\text{pho}} + \Gamma_r] g_{\text{ChR2}} - \varepsilon n_{\text{pho}} g_{\text{refrac}} \\ \dot{g}_{\text{refrac}} &= \Gamma_r g_{\text{ChR2}} - \Gamma_c g_{\text{refrac}} \end{aligned} \quad (2)$$

We identify the state g_{ChR2} as the channelrhodopsin gating variable and integrate it into a well-characterized ventricular cell model (ten Tusscher et al., 2004; Wong et al., 2011) characterized through a total of $n_{\text{gate}} = 14$ gating variables as illustrated in Fig. 5:

$$g_{\text{gate}} = [g_m, g_h, g_j, g_{\text{ChR2}}, g_{\text{xr1}}, g_{\text{xr2}}, g_{\text{xs}}, g_r, g_s, g_d, g_f, g_{\text{K1}\infty}, g_{\text{fCa}}, g_g] \quad (3)$$

In particular, these are the sodium activation gate g_m , the fast and slow sodium inactivation gates g_h and g_j , the channelrhodopsin activation gate g_{ChR2} , the rapid delayed rectifier activation and inactivation gates g_{xr1} and g_{xr2} , the slow delayed rectifier activation gate g_{xs} , the transient potassium activation and inactivation gates g_r and g_s , the long-lasting L-type calcium channel activation and inactivation gates g_d , g_f , and g_{fCa} , and the calcium release activation gate g_g . The gating variables are parameterized in terms of the transmembrane potential ϕ , the ionic concentrations c_{ion} , and the gating variables g_{gate} themselves. Their evolution is governed by classic Hodgkin–Huxley type equations,

$$\dot{g}_{\text{gate}} = \frac{1}{\tau_{\text{gate}}(\phi)} [g_{\text{gate}}^{\infty}(\phi, c_{\text{ion}}) - g_{\text{gate}}] \quad (4)$$

each characterized through a steady state value g_{gate}^{∞} and a time constant τ_{gate} for reaching this steady state (Wong et al., 2011). Both are usually exponential functions of the transmembrane potential ϕ , see Appendix for details. Fig. 6 illustrates the temporal evolution of all $n_{\text{gate}} = 14$ gating variables for the conventional cell, electrically stimulated for 1 ms, dashed black lines, and for the genetically engineered cell, light stimulated for 30 ms, solid blue lines. Overall, the gating variables of the conventional cell and the genetically engineered cell display a similar behavior. The g_{ChR2} gate is, of course, only active for the photosensitive cell.

3. Mathematical model of ionic currents

The channelrhodopsin gating variable g_{ChR2} introduced in the previous section governs the channelrhodopsin photocurrent I_{ChR2} , for which we make the following ansatz.

$$I_{\text{ChR2}} = C_{\text{ChR2}} g_{\text{ChR2}} [\phi - \phi_{\text{ChR2}}] \quad (5)$$

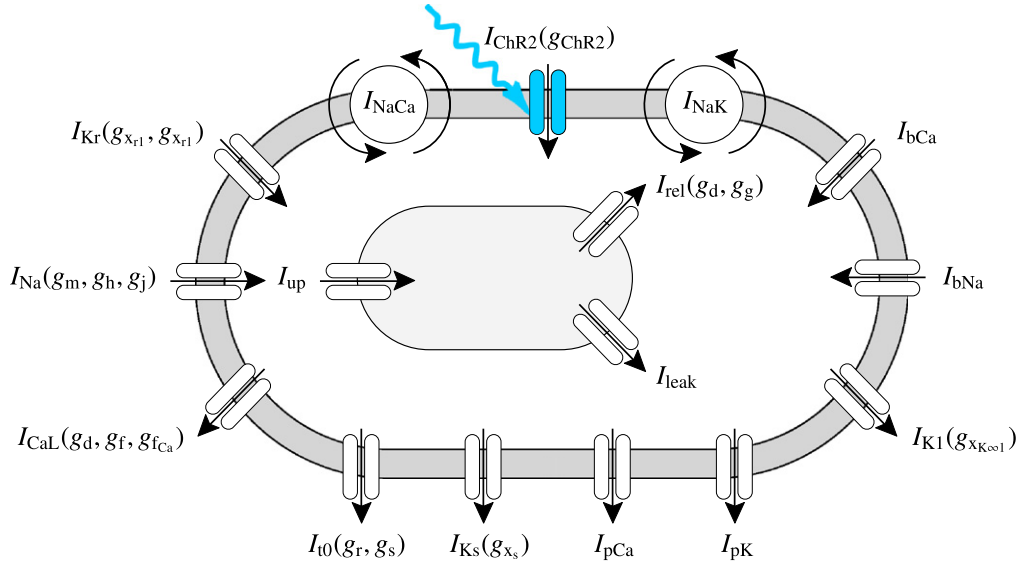


Fig. 5. Genetically engineered light sensitive cardiac cell. The electrophysiology of the cell is characterized in terms of $n_{\text{ion}} = 4$ ion concentrations, the intracellular sodium, potassium, and calcium concentrations and the calcium concentration in the sarcoplasmic reticulum. Ion concentrations are controlled through $n_{\text{crit}} = 16$ ionic currents, where we have enhanced the conventional cell model (ten Tusscher et al., 2004; Wong et al., 2011) with the channelrhodopsin photocurrent I_{ChR2} , here shown in blue (Abilez et al., 2011). The channels are governed by $n_{\text{gate}} = 14$ gating variables, where we have added the channelrhodopsin gating variable g_{ChR2} to characterize the cell's response to photostimulation. (For interpretation of the references to color in this figure legend, the reader is referred to the web version of this article.)

This implies that in our current model, the effects of conduction C_{ChR2} and photostimulation g_{ChR2} on the photocurrent I_{ChR2} are separable. This assumption is sufficient to accurately capture most phenomena reported in the literature (Abilez et al., 2011; Ishizuka et al., 2006). Some more advanced four state models suggest the use of rate variables with dependence on light intensity to finetune of the photocurrent (Nikolic et al., 2009). However, because of the lack of experimental data, it is currently unclear whether these electrical potential effects are truly significant. In our model, the channelrhodopsin conductance

$$C_{\text{ChR2}} = \frac{1}{g_{\text{ChR2}}^{\infty} [\phi_{\text{clamp}} - \phi_{\text{ChR2}}]} I_{\text{ChR2}}^{\infty} \quad (6)$$

is expressed in terms of a quadratic polynomial, which we have identified to $I_{\text{ChR2}}^{\infty} / [\phi_{\text{clamp}} - \phi_{\text{ChR2}}] = 0.000266\phi^2 - 0.003658\phi + 0.498819$ using a least squares fit. With a plateau value g_{ChR2}^{∞} according to Nikolic et al. (2006)

$$g_{\text{ChR2}}^{\infty} = \frac{\varepsilon n_{\text{pho}} \Gamma_c}{\varepsilon n_{\text{pho}} [\Gamma_r + \Gamma_c] + \Gamma_r \Gamma_c} \quad (7)$$

i.e., in our case $g_{\text{ChR2}}^{\infty} = 0.05283$, the conductance becomes $C_{\text{ChR2}} = [0.05\phi^2 - 0.0692\phi + 9.442]$. Moreover, ϕ_{ChR2} is the reversal potential of channelrhodopsin,

$$\phi_{\text{ChR2}} = \phi_{\text{Na}} - \tilde{\phi}_{\text{Na}} \quad (8)$$

which we approximate as the difference of the concentration-dependent reversal potential for sodium ϕ_{Na} and the experimental reversal potential $\tilde{\phi}_{\text{Na}}$:

$$\phi_{\text{Na}} = \frac{RT}{ZF} \log \left(\frac{c_{\text{Na}}^e}{c_{\text{Na}}^i} \right) \quad \text{and} \quad \tilde{\phi}_{\text{Na}} = \frac{RT}{ZF} \log \left(\frac{\tilde{c}_{\text{Na}}^e}{\tilde{c}_{\text{Na}}^i} \right) + \tilde{\phi}_{\text{Na},0} \quad (9)$$

Here, we choose $c_{\text{Na}}^e = 153$ mM (Ishizuka et al., 2006) and $c_{\text{Na}}^i = 11.6$ mM, calibrated to match the experimental reversal potential of channelrhodopsin, and $\tilde{c}_{\text{Na}}^e = 140$ mM, $\tilde{c}_{\text{Na}}^i = 11.6$ mM, and $\tilde{\phi}_{\text{Na},0} = 1.79$ mV. Accordingly, $\phi_{\text{ChR2}} = [RT]/[ZF] [\log(c_{\text{Na}}^e/c_{\text{Na}}^i) - \log(\tilde{c}_{\text{Na}}^e/\tilde{c}_{\text{Na}}^i) + \tilde{\phi}_{\text{Na},0}]$. In contrast to our previous approach, where we have photostimulated an atrial nodal cell (Abilez et al., 2011), we now integrate the channelrhodopsin photocurrent I_{ChR2} into our conventional ventricular cell model (ten Tusscher et al., 2004; Wong et al., 2011), defined through a total of $n_{\text{crit}} = 16$ ionic currents, see Fig. 5.

$$I_{\text{crit}} = [I_{\text{Na}}, I_{\text{bNa}}, I_{\text{NaK}}, I_{\text{NaCa}}, I_{\text{ChR2}}, I_{\text{K1}}, I_{\text{Kr}}, I_{\text{Ks}}, I_{\text{pK}}, I_{\text{t0}}, I_{\text{CaL}}, I_{\text{bCa}}, I_{\text{pCa}}, I_{\text{leak}}, I_{\text{up}}, I_{\text{rel}}] \quad (10)$$

Mathematically speaking, these currents are functions of the transmembrane potential ϕ , the individual gating variables g_{gate} , and the ion concentrations c_{ion} :

$$I_{\text{crit}} = I_{\text{crit}}(\phi, g_{\text{gate}}, c_{\text{ion}}) \quad (11)$$

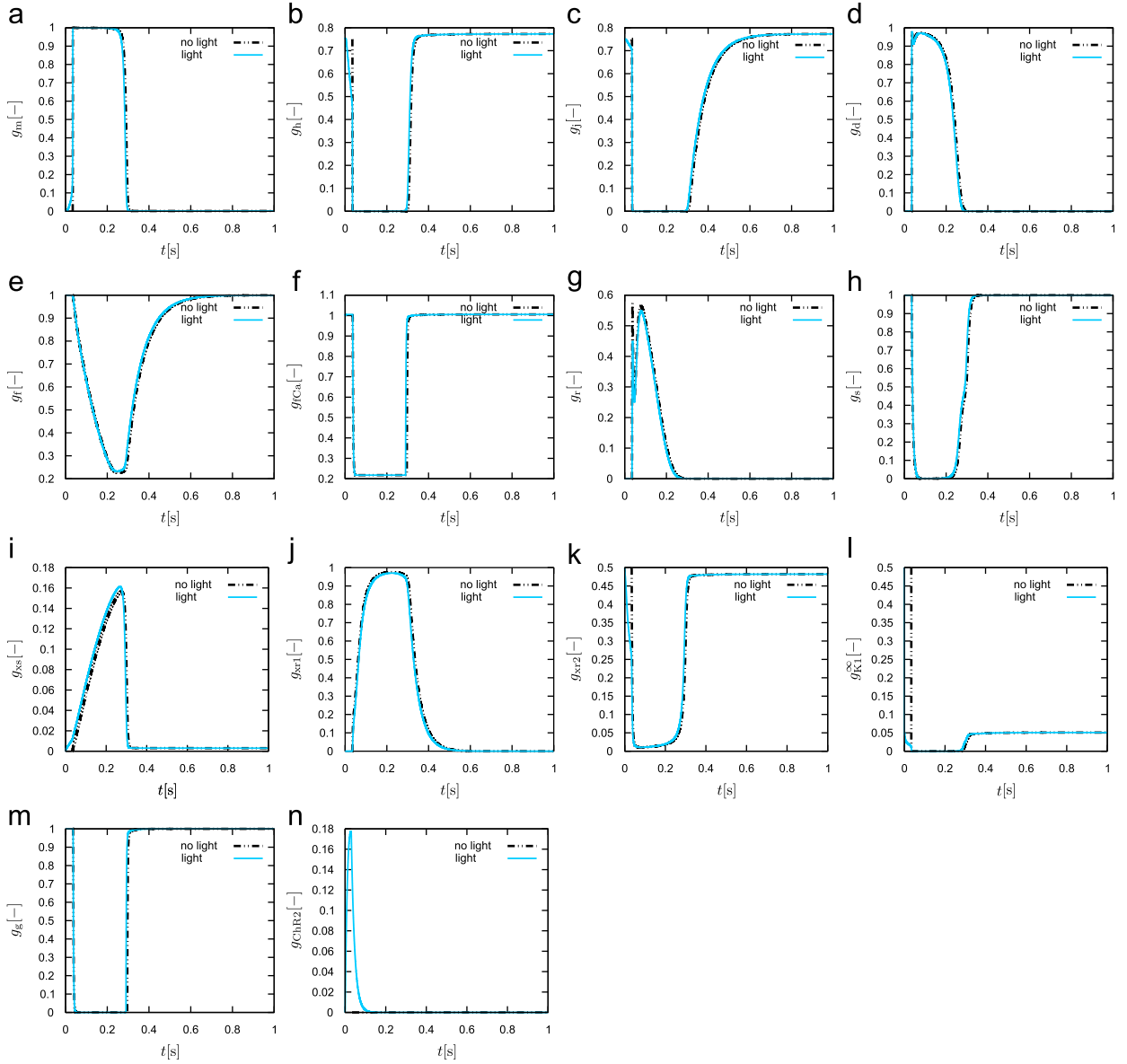


Fig. 6. Genetically engineered light sensitive cardiac cell stimulated conventionally with an electric field, dashed lines, and optically with light, solid lines. Temporal evolution of sodium activation gate g_m , fast sodium inactivation gate g_h , slow sodium inactivation gate g_l , L-type calcium activation gate g_a , L-type calcium inactivation gate g_r , intracellular calcium dependent calcium inactivation gate g_{icca} transient outward activation gate g_s , transient outward inactivation gate g_{ss} , slow delayed rectifier gate g_{ss} , rapid delayed rectifier activation gate g_{xr1} , rapid delayed rectifier inactivation gate g_{xr2} , inward rectification factor g_{k1} , calcium-dependent inactivation gate g_g , and channelrhodospin activation gate g_{chR2} . The gating dynamics for the electrically stimulated cell have been delayed by 34 ms for the purposes of comparison against the optically stimulated cell.

In particular, these are the fast sodium current I_{Na} , the background sodium current I_{bNa} , the sodium potassium pump current I_{NaK} , the sodium calcium exchanger current I_{NaCa} , the channelrhodospin photocurrent I_{ChR2} , the inward rectifier current I_{K1} , the rapid delayed rectifier current I_{Kr} , the slow delayed rectifier current I_{Ks} , the plateau potassium current I_{pK} , the transient outward current I_{to} , the L-type calcium current I_{CaL} , the background calcium current I_{bCa} , the plateau calcium current I_{pCa} , the leakage current I_{leak} , and sarcoplasmic reticulum uptake and release currents I_{up} and I_{rel} , see Appendix for details. Fig. 7 illustrates the temporal evolution of all $n_{crt} = 16$ currents for the conventional cell, electrically stimulated for 1 ms, dashed black lines, and for the genetically engineered cell, light stimulated for 30 ms, solid blue lines. Except for the fast sodium current I_{Na} , the currents of the conventional cell and the genetically engineered cell display a relatively similar behavior. Overshoots in the potassium related currents are less pronounced for the photosensitive cell. The channelrhodospin photocurrent I_{ChR2} is, of course, only active for the photosensitive cell.

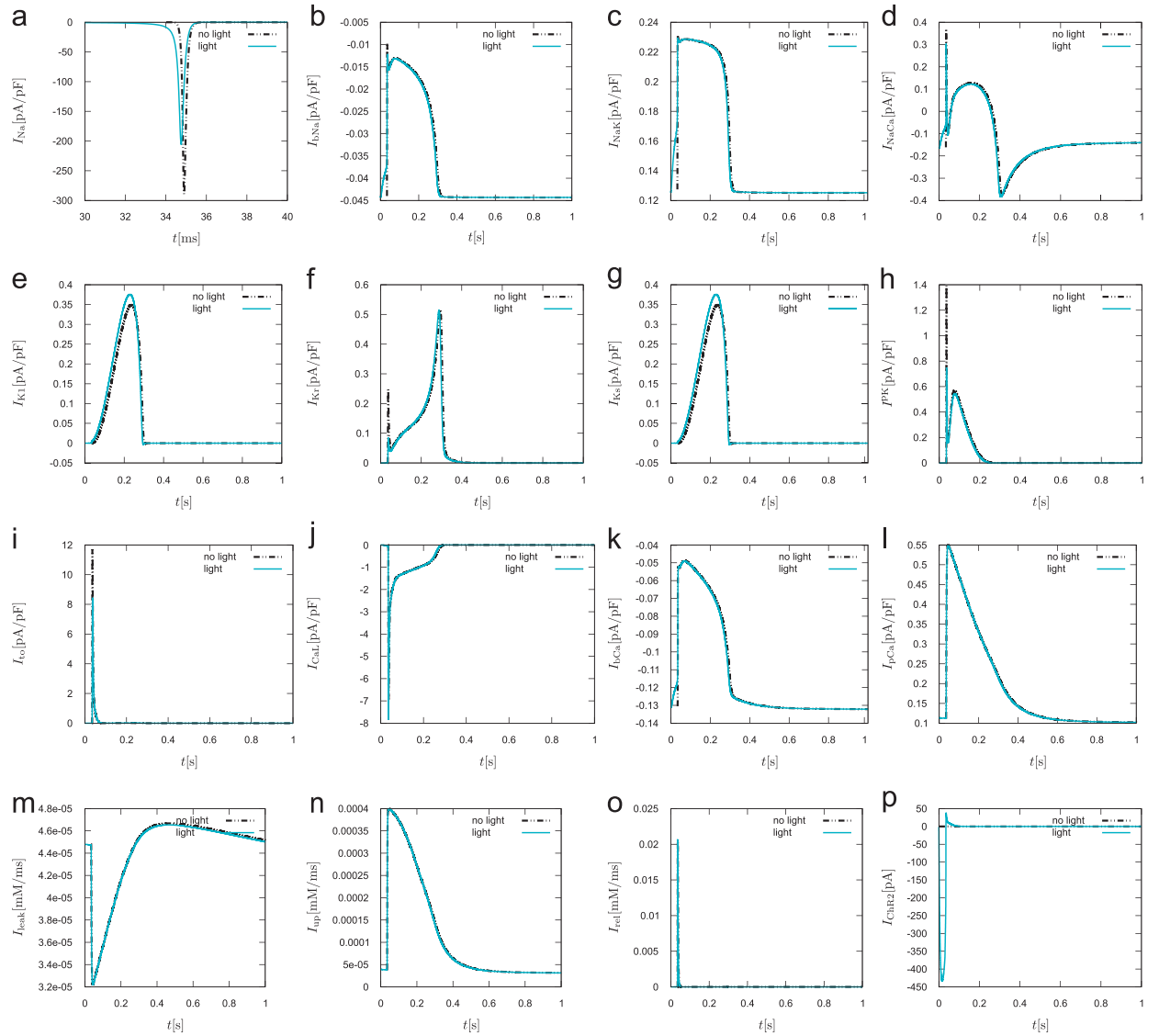


Fig. 7. Genetically engineered light sensitive cardiac cell stimulated conventionally with an electric field, dashed lines, and optically with light, solid lines. Temporal evolution of fast sodium current I_{Na} , background sodium current I_{bNa} , sodium potassium pump current I_{NaK} , sodium calcium exchanger current I_{NaCa} , inward rectifier current I_{K1} , rapid delayed rectifier current I_{Kr} , slow delayed rectifier current I_{Ks} , plateau potassium current I_{PK} , transient outward current I_o , L-type calcium current I_{cal} , background calcium current I_{bCa} , plateau calcium current I_{pCa} , leakage current I_{leak} , sarcoplasmic reticulum uptake current I_{up} , sarcoplasmic reticulum release current I_{rel} , and channelrhodopsin current I_{ChR2} . The current dynamics for the electrically stimulated cell have been delayed by 34 ms for the purposes of comparison against the optically stimulated cell.

4. Mathematical model of ionic concentrations

From a chemical point of view, light induces a channelrhodopsin photocurrent I_{ChR2} , which directly impacts the intracellular sodium concentration c_{Na} ,

$$\dot{c}_{Na} = -\frac{1}{FV} [I_{Na} + I_{bNa} + 3I_{NaCa} + 3I_{NaK} + I_{ChR2}] \quad (12)$$

where V is the cytosolic volume and F is the Faraday constant. The sodium concentration will directly, and indirectly through the resulting changes in the transmembrane potential ϕ , affect all other ionic concentrations in the cell. The biochemistry of our cell model is characterized through $n_{ion} = 4$ ion concentrations,

$$c_{ion} = [c_{Na}, c_{K}, c_{Ca}, c_{Ca}^{ST}] \quad (13)$$

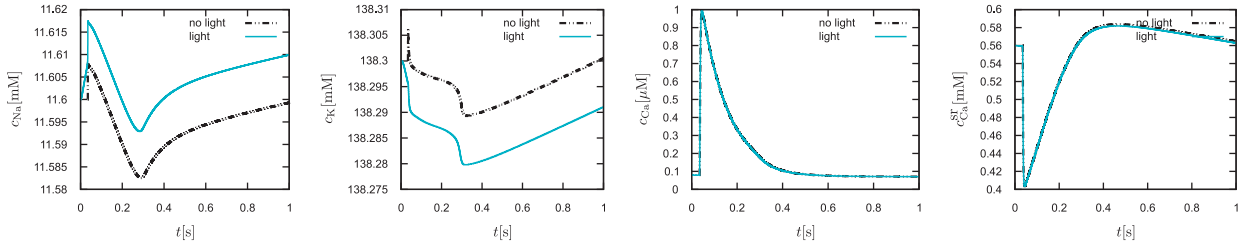


Fig. 8. Genetically engineered light sensitive cardiac cell stimulated conventionally with an electric field, dashed lines, and optically with light, solid lines. Temporal evolution of intracellular sodium c_{Na} , potassium c_K , calcium c_{Ca} concentrations, and calcium concentration c_{Ca}^{sr} in the sarcoplasmic reticulum. The chemical concentration dynamics for the electrically stimulated cell have been delayed by 34 ms for the purposes of comparison against the optically stimulated cell.

where c_{Na} , c_K , and c_{Ca} are the intracellular sodium, potassium, and calcium concentrations, and c_{Ca}^{sr} is the calcium concentration in the sarcoplasmic reticulum. The concentrations obey evolution equations of the following format:

$$\dot{c}_{ion} = f_{ion}(\phi, g_{gate}, c_{ion}) \quad (14)$$

which are parameterized in terms of the transmembrane potential ϕ , the gating variables g_{gate} , and the ion concentrations c_{ion} themselves, see Appendix for details. Fig. 8 illustrates the temporal evolution of all $n_{gate} = 14$ gating variables for the conventional cell, electrically stimulated for 1 ms, dashed black lines, and for the genetically engineered cell, light stimulated for 30 ms, solid blue lines. While the calcium concentrations inside the cell c_{Ca} and in the sarcoplasmic reticulum c_{Ca}^{sr} remain unaffected by photostimulation, the intracellular sodium concentration c_{Na} increases with light. Through the sodium potassium pump current I_{NaK} , this has a direct impact on the intracellular potassium concentration c_K , which decreases upon photostimulation.

5. Mathematical model of action potential propagation

From an electrical point of view, light induces a channelrhodopsin current I_{ChR2} , which directly impacts the sodium concentration c_{Na} , and thus, the action potential propagation ϕ in the heart. Unlike the local ion concentrations for single cells, however, the action potential ϕ is a global field variable (Göktepe and Kuhl, 2009). It propagates from cell to cell via gap junction channels (Jia et al., 2011). We can characterize its spatio-temporal evolution through a nonlinear parabolic second-order partial differential equation

$$\dot{\phi} = f^\phi(\phi, g_{gate}, c_{ion}) + \text{div } \mathbf{q}(\phi) \quad (15)$$

driven by a nonlinear local source term f^ϕ at the single cell level, and by a linear global flux term, $\text{div } \mathbf{q}$, the divergence of the propagation vector \mathbf{q} at the organ level. We identify the local source term

$$f^\phi = -\frac{1}{C} [I_{Na} + I_{bNa} + I_{NaK} + I_{NaCa} + I_{ChR2} + I_{K1} + I_{Kr} + I_{Ks} + I_{pK} + I_{t0} + I_{CaL} + I_{bCa} + I_{pCa}] \quad (16)$$

as the negative sum of all transmembrane currents scaled by the cell membrane capacitance per unit surface area C . To account for the nonlocal nature of propagating excitation waves in the heart, we introduce the propagation vector

$$\mathbf{q} = \mathbf{D} \cdot \nabla \phi \quad (17)$$

through the second-order diffusion tensor \mathbf{D} scaling the gradient of the action potential field $\nabla \phi$. Fig. 9 illustrates the five phases of the action potential ϕ for the conventional cell, electrically stimulated for 1 ms, dashed black lines, and for the genetically engineered cell, light stimulated for 30 ms, solid blue lines. We can clearly see the impact of photostimulation, which requires the entire stimulation period of 30 ms to push the cell beyond its excitation threshold. For visualization purposes, we have shifted the transmembrane potential of the electrical stimulation, dashed lines, by 34 ms, which agrees qualitatively with the time delay of 19.7 ± 3.4 ms reported in the literature (Bruegmann et al., 2010). Beyond the stimulation threshold, both cells display an almost identical electrical response with the characteristic rapid upstroke, early, partial repolarization, plateau, final repolarization, and rest phases. Again, this agrees nicely with experimental findings (Bruegmann et al., 2010).

6. Computational model of light-activated cells

To solve the spatio-temporal problem of electrochemical coupling (4), (14), and (15) for the gating variables g_{gate} , the intracellular ion concentrations c_{ion} , and the transmembrane potential ϕ , we apply a finite difference scheme in time and a finite element scheme in space. Due to the global nature of the membrane potential introduced through the diffusion term $\text{div } \mathbf{q}(\phi)$, we suggest a C^0 -continuous finite element interpolation for the membrane potential ϕ , while a C^{-1} -continuous interpolation is sufficient for the sets of gating variables g_{gate} and ion concentrations c_{ion} (Göktepe and Kuhl, 2009, 2010). Accordingly, we introduce the membrane potential as global degree of freedom at each finite element node, and the gating

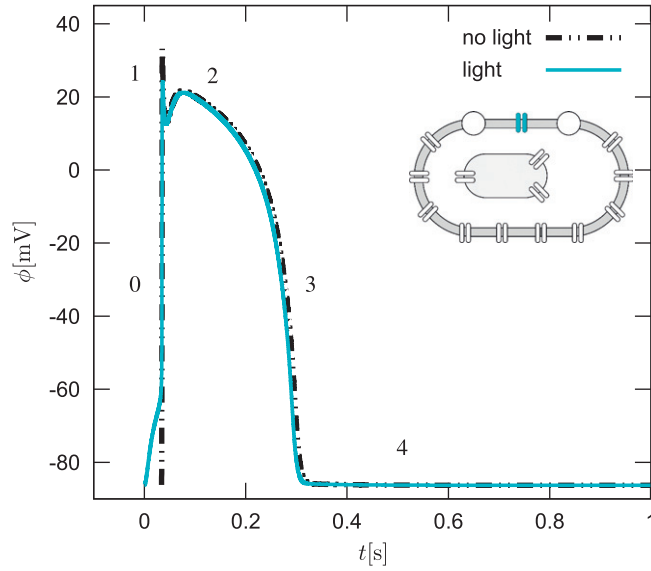


Fig. 9. Genetically engineered light sensitive cardiac cell stimulated conventionally with an electric field, dashed lines, and optically with light, solid lines. Temporal evolution of transmembrane potential ϕ . The characteristic action potential consists of five phases. Phase 0: The rapid upstroke is generated through an influx of positively charged sodium ions. Phase 1: Early, partial repolarization is initiated through the efflux of positively charged potassium ions. Phase 2: During the plateau, the net influx of positively charged calcium ions is balanced by the efflux of positively charged potassium ions. Phase 3: Final repolarization begins when the efflux of potassium ions exceeds the influx of calcium ions. Phase 4: Throughout the interval between end of repolarization and the beginning of the next cycle the cell is at rest. The transmembrane potential for the electrically stimulated cell has been delayed by 34 ms for the purposes of comparison against the optically stimulated cell. This delay agrees nicely with the time delay of activation of 19.7 ± 3.4 ms reported in the literature (Bruegmann et al., 2010).

variables and ion concentrations locally on the integration point level (Wong et al., 2011). We solve the resulting staggered system with an incremental iterative Newton–Raphson solution procedure based on the consistent linearization of the discrete excitation problem (Chen et al., 2011; Dal et al., 2011; Göktepe et al., 2010).

6.1. Chemical problem: local discretization on the integration point level

We typically initialize the chemical state variables at t_0 with their resting state values. Our goal is to determine the chemical state variables, i.e., the $n_{\text{gate}} = 14$ gating variables g_{gate} and the $n_{\text{ion}} = 4$ ion concentrations c_{ion} of the current time step t for a given action potential ϕ at t , and known chemical state variables from the previous time step t^n . For the temporal discretization, we partition the time interval of interest \mathcal{T} into n_{stp} subintervals $[t^n, t^{n+1}]$ as $\mathcal{T} = \bigcup_{n=0}^{n_{\text{stp}}-1} [t^n, t^{n+1}]$ and apply a standard backward Euler time integration scheme in combination with a finite difference approximation of the first-order time derivatives $\dot{g}_{\text{gate}}\phi$ and \dot{c}_{ion} :

$$\dot{g}_{\text{gate}} = [g_{\text{gate}} - g_{\text{gate}}^n] / \Delta t \quad \text{and} \quad \dot{c}_{\text{ion}} = [c_{\text{ion}} - c_{\text{ion}}^n] / \Delta t \quad (18)$$

Here and from now on, we omit the index $(\cdot)^{n+1}$ for the sake of clarity, and introduce the common abbreviation $\Delta t := t - t^n > 0$ for the current time increment. This allows us to transform the linear set of gating equations (4) into a set of update equations for the gating variables g_{gate} at the current time step t :

$$g_{\text{gate}} = g_{\text{gate}}^n + \frac{1}{\tau_{\text{gate}}(\phi)} [g_{\text{gate}}^\infty(\phi) - g_{\text{gate}}] \Delta t \quad (19)$$

The gating variables define the $n_{\text{crt}} = 16$ ionic currents $I_{\text{crt}}(\phi, g_{\text{gate}}, c_{\text{ion}})$, which alter the $n_{\text{ion}} = 4$ intracellular ion concentrations c_{ion} . With the help of the finite difference approximation (18), we reformulate the nonlinear set of concentration equations (14) in the following residual format:

$$R_{\text{ion}}^c = c_{\text{ion}} - c_{\text{ion}}^n - f_{\text{ion}}^c(\phi, g_{\text{gate}}, c_{\text{ion}}) \Delta t \doteq 0 \quad (20)$$

To obtain the $n_{\text{ion}} \times n_{\text{ion}}$ iteration matrix $K_{\text{ion ion}}^c$ for the local Newton iteration on the integration point level, we linearize the discrete algorithmic residual:

$$K_{\text{ion}}^c = d_{c_{\text{ion}}} R_{\text{ion}}^c = 1 - d_{c_{\text{ion}}} f_{\text{ion}}^c \quad (21)$$

At the end of each Newton iteration, we update the set of ion concentrations $c_{\text{ion}} \leftarrow c_{\text{ion}} - [K_{\text{ion}}^c]^{-1} R_{\text{ion}}^c$, the set of gating variables $g_{\text{gate}} \leftarrow g_{\text{gate}} + [g_{\text{gate}}^\infty(\phi) - g_{\text{gate}}] \Delta t / \tau$ and the set of ionic currents $I_{\text{crt}} \leftarrow I_{\text{crt}}(\phi, g_{\text{gate}}, c_{\text{ion}})$, and continue to iterate locally

until we achieve convergence. This local inner loop can be understood as a modern implicit version of the iterative update procedure of the original [Rush and Larsen \(1978\)](#) algorithm.

6.2. Electrical problem: global discretization on the node point level

To evaluate the action potential ϕ on the node point level, we transform the electrical problem (15) into its residual format

$$\mathbf{R}^\phi = \dot{\phi} - \text{div}(\mathbf{q}) - f^\phi \doteq 0 \tag{22}$$

in the domain of interest \mathcal{B} . We complement this initial boundary value problem with the corresponding Dirichlet and Neumann boundary conditions $\phi = \bar{\phi}$ on $\partial\mathcal{B}_\phi$ and $\mathbf{q} \cdot \mathbf{n} = \bar{q}$ on $\partial\mathcal{B}_q$, typically using homogeneous Neumann boundary conditions $\mathbf{q} \cdot \mathbf{n} = 0$ on the entire boundary $\partial\mathcal{B}$. As initial conditions, $\phi_0(x) = \phi(x, t_0)$ in \mathcal{B} , we simply set the transmembrane potential to its resting state. We obtain the weak form of the electrical residual (22) through the integration over the domain \mathcal{B} , the standard integration by parts, and the inclusion of the Neumann boundary conditions. For the spatial discretization, we discretize the domain of interest \mathcal{B} with n_{el} finite elements \mathcal{B}^e as $\mathcal{B} = \bigcup_{e=1}^{n_{el}} \mathcal{B}^e$ and apply the standard isoparametric concept to interpolate the trial functions ϕ and the test functions $\delta\phi$:

$$\delta\phi = \sum_{i=1}^{n_{en}} N^i \delta\phi_i, \quad \phi = \sum_{j=1}^{n_{en}} N^j \phi_j \tag{23}$$

Here, N are the standard shape functions on the element level and $i, j = 1, \dots, n_{en}$ are the n_{en} element nodes. For the temporal discretization, we suggest a finite difference approximation of the first-order time derivative $\dot{\phi}$,

$$\dot{\phi} = [\phi - \phi^n] / \Delta t \tag{24}$$

in combination with a standard backward Euler time integration scheme. Using the discretizations in space (23) and time (24), we can introduce the discrete algorithmic residual \mathbf{R}_I^ϕ :

$$\mathbf{R}_I^\phi = \mathbf{A}_{e=1}^{n_{el}} \int_{\mathcal{B}^e} N^i \frac{\phi - \phi^n}{\Delta t} + \nabla N^i \cdot \mathbf{q} \, dV - \int_{\partial\mathcal{B}_q^e} N^i \bar{q} \, dA - \int_{\mathcal{B}^e} N^i f^\phi \, dV \doteq 0 \tag{25}$$

The operator \mathbf{A} symbolizes the assembly of all element contributions at the element nodes $i = 1, \dots, n_{en}$ to the overall residual at the global node points $l = 1, \dots, n_{nd}$. To solve the discrete system of nonlinear equations (25), we suggest an incremental iterative Newton Raphson solution technique based on the consistent linearization of the residual, which introduces the global iteration matrix \mathbf{K}_{IJ}^ϕ .

$$\mathbf{K}_{IJ}^\phi = \mathbf{d}_{\phi_j} \mathbf{R}_I^\phi = \mathbf{A}_{e=1}^{n_{el}} \int_{\mathcal{B}^e} N^i \frac{1}{\Delta t} N^j + \nabla N^i \cdot \mathbf{D} \cdot \nabla N^j - N^i \mathbf{d}_{\phi_j} f^\phi N^j \, dV \tag{26}$$

For each incremental iteration, we update the global vector of unknowns $\phi_l \leftarrow \phi_l - \sum_{j=1}^{n_{nd}} \mathbf{K}_{IJ}^{\phi-1} \mathbf{R}_j^\phi$ at all $l = 1, \dots, n_{nd}$ global nodes. At convergence of the local Newton iteration, i.e., at chemical equilibrium, we can evaluate the source term $f^\phi(\phi, g_{\text{gate}}, c_{\text{ion}})$ for the electrical problem (25), and its linearization $\mathbf{d}_{\phi_j} f^\phi(\phi, g_{\text{gate}}, c_{\text{ion}})$ for the global Newton iteration (26). The use of a fully monolithic implicit solution algorithm allows us to apply an adaptive time stepping procedure, for which the time step size is automatically adjusted in response to the number of Newton iterations towards global equilibrium ([Wong et al., 2011](#)). In principle, the above equations for \mathbf{R}_I^ϕ and \mathbf{K}_{IJ}^ϕ are generically portable and can interface with any commercially available finite element package. Here, we embed the proposed algorithm in the general multipurpose nonlinear finite element program FEAP ([Taylor, 2011](#)).

7. Computational model of a human heart

To illustrate the features of the proposed algorithm, we model the photostimulation of a human heart stimulated at three different pacing sites. We create a patient-specific heart model from magnetic resonance images taken at different depths along the heart's long axis, see [Fig. 10](#). On these two-dimensional slices, we use semi-automated image processing tools to section the regions of the cardiac muscle. From the raw and noisy grayscale images, we create monochrome images with sharply defined boundaries using thresholding and binary masking. From the resulting black and white slices, we generate three preliminary triangular surface meshes, one for the outer surface and one for the inner surface of each ventricle. Finally, we convert the surface meshes into a tetrahedral volume mesh consisting of 3129 nodes and 11,347 tetrahedral elements ([Kotikanyadanam et al., 2010](#)), see [Fig. 10](#).

We virtually inject our genetically engineered, light sensitive cardiac cells into different regions of the heart ([Modi et al., 2011](#)), and model all other cells as conventional cardiac muscle cells ([ten Tusscher et al., 2004](#); [Wong et al., 2011](#)). The former group of cells possesses the additional channelrhodopsin current I_{ChR2} , while the latter does not. Following the literature, we model cell injection by modifying the material properties of the myocardial wall at the injection sites ([Wenk et al., 2011](#)). Here, these regions span a volume of approximately 0.02 cm^3 , which is roughly the size of the $0.6 \times 0.3 \times 0.1 \text{ cm}^3$ large atrioventricular node in humans, corresponding to approximately 10^7 cells ([James, 1961](#)). To

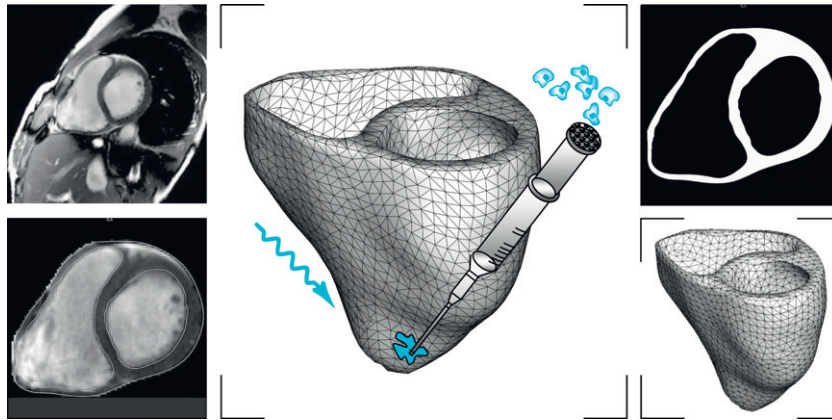


Fig. 10. Virtual injection of genetically engineered light sensitive cardiac cells into a human heart. Magnetic resonance imaging generates a sequence of two-dimensional images at different depths (top, left). We segment cardiac muscle tissue semi-manually using standard image processing techniques (bottom, left). Thresholding and binary masking convert the raw grayscale images to monochrome images with sharply defined boundaries (top, right). From these slices, we create a preliminary triangular surface mesh and converted it into the final tetrahedral volume mesh consisting of 3129 nodes and 11,347 tetrahedral elements (bottom, right). Last, we virtually inject photosensitive cells into different regions of the heart and stimulated with light (middle).

initiate electrical activation, we photostimulate the light sensitive cells for a period of 30 ms with blue light, then turn off the light, and record the action potential propagation across the heart.

7.1. Atrioventricular node pacing through photostimulation

Fig. 11 illustrates the activation profile in response to atrioventricular node pacing through photostimulation. To reproduce the native activation sequence of the human heart, we virtually inject photosensitive cells into the basal septal region, the location of the atrioventricular node, and pace them with blue light. A depolarization wave forms in the region of the atrioventricular node, travels down the septum, and activates the left and right ventricles. When comparing the temporal evolution of the transmembrane potential ϕ , top row, with the different ion concentrations c_{Na} , c_K , and c_{Ca} , lower rows, we observe that the sodium concentration changes first, with a sharp front, followed by changes in the potassium and calcium concentrations, with smoother fronts. These observations are in agreement with the temporal evolution of the local ion concentrations illustrated in Fig. 8. After approximately 50 ms, the entire heart is depolarized. The transmembrane potential ϕ has changed from approximately -80 mV to $+20$ mV.

7.2. Apical pacing through photostimulation

Fig. 12 shows the response of the heart to apical pacing through photostimulation. The right ventricular apex has traditionally been the most prominent pacing site, providing a stable lead position associated with few complications. To predict the activation sequence in response to apical pacing, we virtually inject photosensitive cells into the apex, stimulate them with light for 30 ms, turn off the light, and monitor the electrical and chemical fields. As the transmembrane potential profile indicates, a depolarization wave forms at the apex, travels up towards the base, and activates the septum and both ventricles simultaneously. Again, we observe the rapid increase in the intracellular sodium concentration c_{Na} causing the heart to depolarize. The transmembrane potential changes from -80 mV to $+20$ mV within the first 50 ms of the cycle, until the heart is completely depolarized. The intracellular calcium concentration c_{Ca} follows smoothly, while the intracellular potassium concentration c_K changes only in the later stages.

7.3. Biventricular pacing through photostimulation

Fig. 13 displays the activation of the heart, photostimulated through bi-ventricular pacing. Biventricular pacing is a common pacing strategy in patients with heart failure for which both ventricles do not contract synchronously. To simulate biventricular pacing, we virtually inject photosensitive cells into the lateral walls of the left and right ventricles and pace both locations simultaneously. In response to photostimulation, two depolarization waves form one at each pacing site. The waves travel along the ventricles to finally activate the apex and the septum. Again, during depolarization, the transmembrane potential profile ϕ closely follows the intracellular sodium concentration c_{Na} , which triggers the rapid upstroke of the action potential, while the intracellular calcium concentration c_{Ca} follows slightly later with a smoother propagation front.

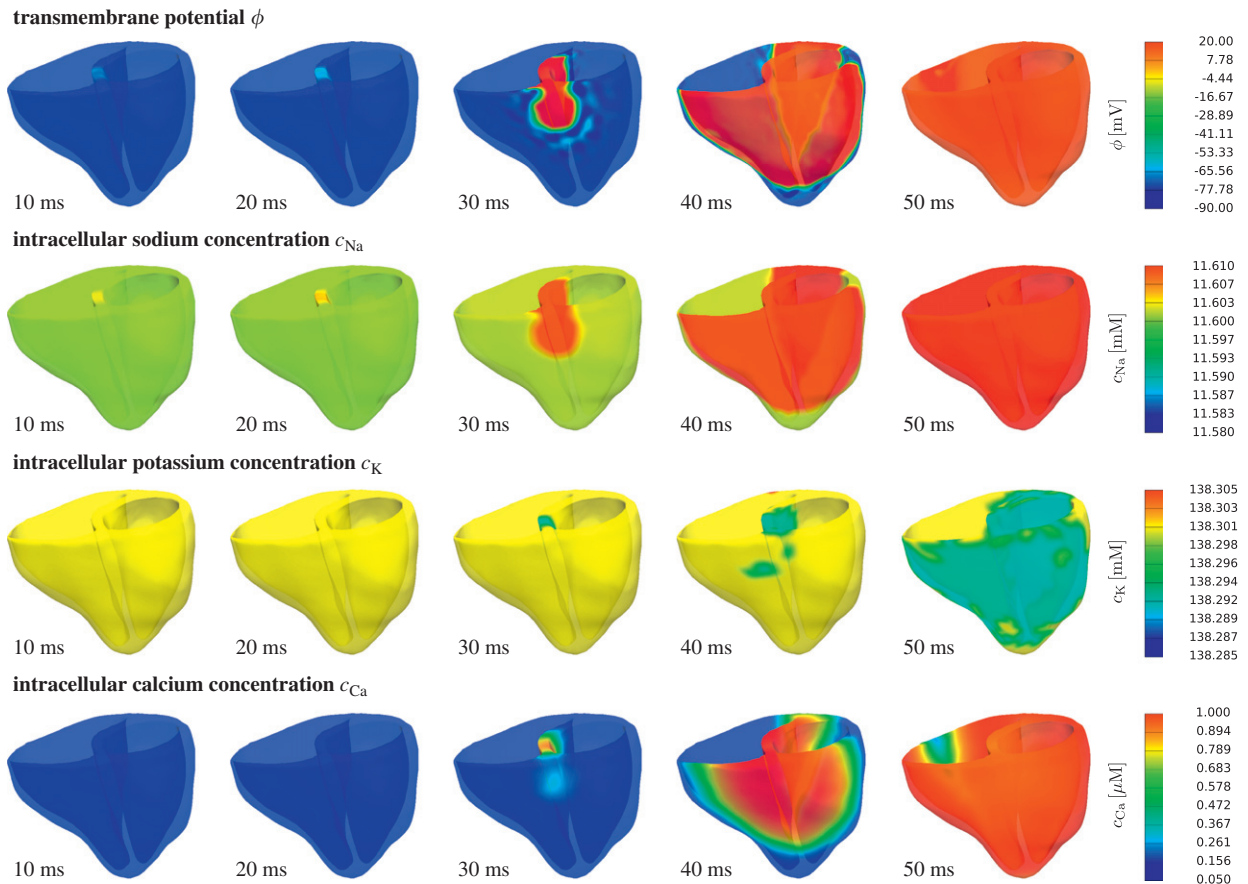


Fig. 11. Photostimulation of a human heart. Spatio-temporal evolution of transmembrane potential ϕ , intracellular sodium c_{Na} , potassium c_K , and calcium c_{Ca} concentrations for atrioventricular node paced heart. Photosensitive cells are virtually injected into the basal region of the septum, while all other regions are modeled as conventional cardiac muscle cells. A depolarization wave forms at the atrioventricular node, travels down the septum, and activates the left and right ventricles.

8. Discussion

8.1. Comparison with the literature

Within the past decade, optogenetics has become a tremendously active field of research (Deisseroth, 2011), however, little is known about its impact on cardiac cells, neither in isolation nor in the cardiac system. Since the channelrhodopsin photocycle itself is relatively well established from intense studies of the neuronal system (Nikolic et al., 2006, 2009), we simply adopt the kinetics of a well-characterized three-state photocycle model (Hegemann et al., 2005; Nagel et al., 2003). Creating a cellular model system that expresses Channelrhodopsin-2 allows us to validate its photocurrent using whole cell patch-clamp (Jia et al., 2011) or multielectrode array recordings (Bruegmann et al., 2010). Using both techniques, we have recently demonstrated that our cell model is capable of reliably reproducing experimentally measured photo-stimulation amplitudes, pulse widths, and frequencies from single cell recordings (Abilez et al., 2011). In this paper, for the first time, we quantify the impact of photostimulation in side-by-side comparisons between conventional cells, electrically stimulated for 1 ms, and genetically engineered cells, optically stimulated for 30 ms, see Figs. 6–9. The gating variables in Fig. 6 can be understood as internal variables, which cannot be measured experimentally. The ionic currents in Fig. 7 can be extracted experimentally from a series of voltage and current clamp recordings using drugs to selectively block the activity of different combinations of channels. Although theoretically possible, for optogenetically engineered cells, typically only the channelrhodopsin photocurrent is measured experimentally. Its indirect impact on all other currents, however, has not been characterized systematically to date. The ion concentrations in Fig. 8 could potentially be measured experimentally, however, for optogenetically engineered cells, this has not been done to date. Unfortunately, only three groups worldwide have reported the use of optogenetics to manipulate the cardiac system, one in zebrafish (Arrenberg et al., 2010), one in transgenic mice (Bruegmann et al., 2010), and one in stem cell derived cardiomyocytes (Abilez et al., 2011). The last study by our own group is the only one that has demonstrated the potential of optogenetics in human heart

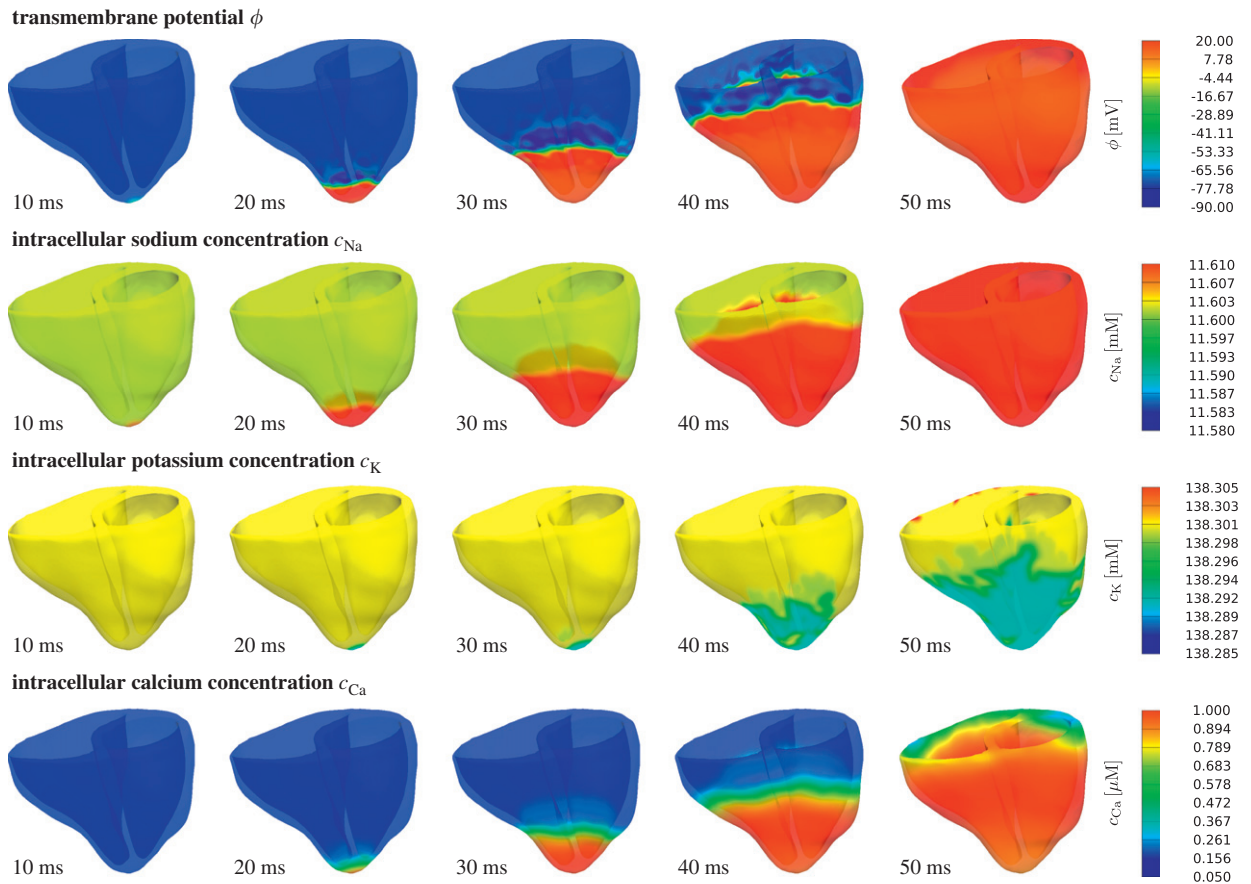


Fig. 12. Photostimulation of a human heart. Spatio-temporal evolution of transmembrane potential ϕ , intracellular sodium c_{Na} , potassium c_K , and calcium c_{Ca} concentrations for apically paced heart. Photosensitive cells are virtually injected into the apex, while all other regions are modeled as conventional cardiac muscle cells. A depolarization wave forms at the apex, travels up, and activates the septum and both ventricles simultaneously.

cells. This underlines the importance of computational models, which provide easy access to ion channel dynamics and ionic concentrations, both in healthy and diseased conditions.

The transmembrane potential in Fig. 9 could potentially be extracted from patch clamp or microelectrode array recordings. Here, for the selected light intensity, we find 30 ms to be the minimum light exposure time to evoke a standard action potential. For photostimulation just slightly above this threshold, we identify the time delay between electrical stimulation and photostimulation to be 34 ms, which agrees nicely with the values of 19.7 ± 3.4 ms reported in the literature (Bruegmann et al., 2010). Although not explicitly reported here, in agreement with the literature, we observe a decrease in activation delay for increased light intensities (Bruegmann et al., 2010). Beyond the stimulation threshold, however, electrically and optically activated cells display an almost identical electrophysiology with the characteristic rapid upstroke, early, partial repolarization, a pronounced plateau, a final repolarization, and a return to the resting phase, see Fig. 9. Again, this agrees nicely with experimental findings, which report that channelrhodopsin expression in murine embryonic stem cells is not associated with additional leak currents, or changes in the resting membrane potential, membrane resistance, and action potential duration (Bruegmann et al., 2010).

A first qualitative study in zebrafish has demonstrated that optogenetic tools can, in principle, be used to control the cardiac system *in vivo* (Arrenberg et al., 2010). In that study, optical perturbation of genetically engineered pacemaker cells was entirely reversible. This agrees nicely with our optically stimulated transmembrane potential returning smoothly to its resting state, see Fig. 9. The study also showed that only few genetically engineered cells are needed to deliver a sufficient optical stimulus in zebrafish hearts (Arrenberg et al., 2010). In our human heart, we virtually inject approximately 10^7 cells covering a volume of 0.02 cm^3 , which is roughly the size of the atrioventricular node in humans, see Fig. 10. In agreement with an *in vivo* study in transgenic mice (Bruegmann et al., 2010), we observe that smaller cell volumes require either increased light intensities or longer stimulation times. Similar to the reported activation delays of 12.2 ± 3.7 ms and 9.3 ± 2.2 ms upon atrial and ventricular photostimulation in mice (Bruegmann et al., 2010), we observe an activation delay of 19.5 ms when comparing our light activated heart in Fig. 11 with previous simulations of native activation sequences (Kotikanyadanam et al., 2010; Tsamis et al., 2011) and electrical pacing (Wong et al., 2011).

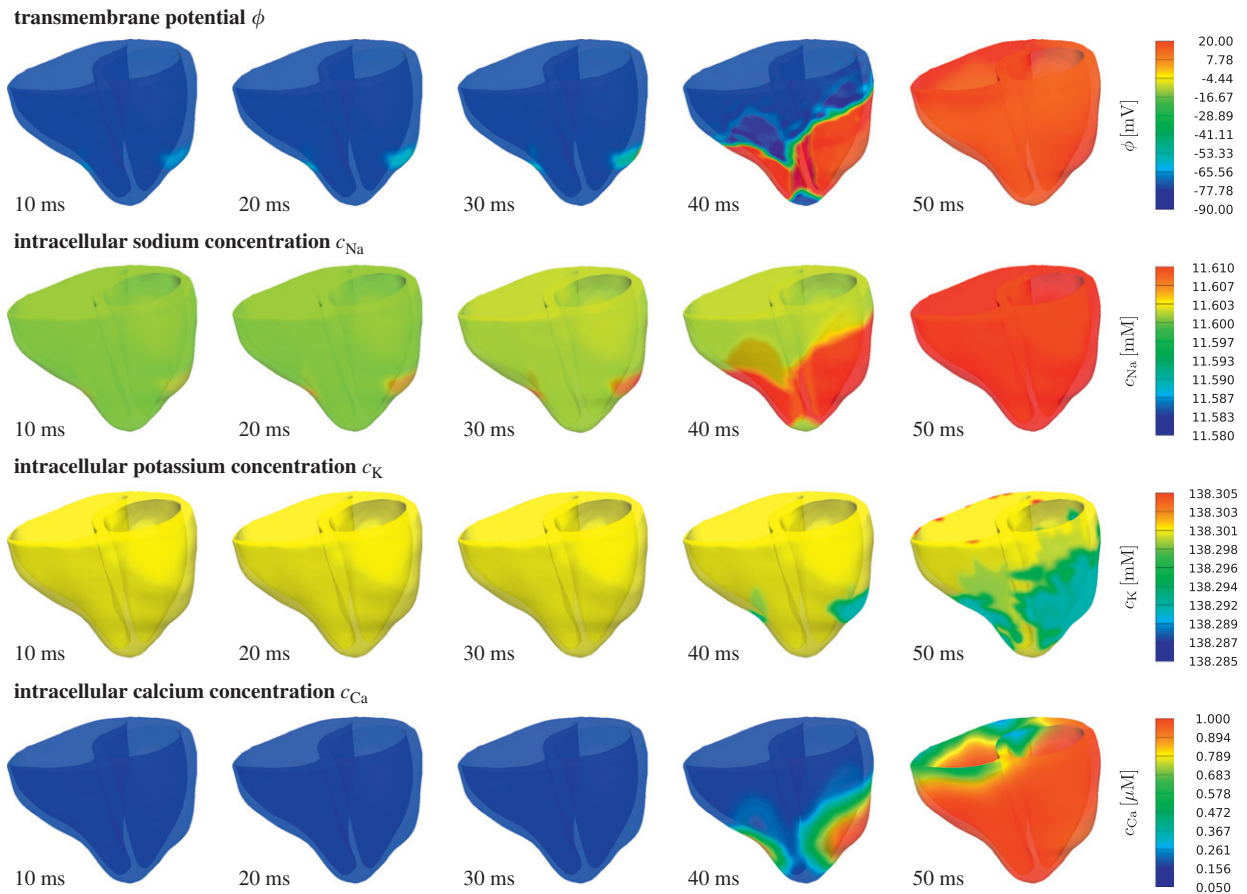


Fig. 13. Photostimulation of a human heart. Spatio-temporal evolution of transmembrane potential ϕ , intracellular sodium c_{Na} , potassium c_K , and calcium c_{Ca} concentrations for bi-ventricularly paced heart. Photosensitive cells are virtually injected into the lateral walls of the left and right ventricles, while all other regions are modeled as conventional cardiac muscle cells. Two depolarization waves form in the lateral left and right ventricular walls to travel along the ventricles and activate the apex and the septum.

Overall, because of the inherent frequency mismatch in rodents and humans, the complete *in vivo* validation of our model remains challenging, and can only be addressed satisfactorily by means of large animal models. This is, however, a generic limitation of the clinical translational character of cardiac optogenetics in general. Large animal models would also allow us to quantify the impact of optogenetic stimulation on cardiac function *in vivo*. In a previous study, we have demonstrated how light can be turned into force using optogenetic tools *in vitro* (Abilez et al., 2011). A related study by another group reported light-induced mechanical strains of up to 4.5% (Jia et al., 2011). We are currently integrating our continuum model for the photoelectrochemistry of living systems into a model for excitation–contraction coupling (Göktepe et al., 2010). This will allow us to characterize the mechanically mediated ionic response of strain-gated ion channels (Reeves et al., 2008; Ursell et al., 2007), and, vice versa, the calcium-mediated mechanical response of the heart (Criscione et al., 2002; Rausch et al., 2011), and its impact on muscle contraction and cardiac function (Givli and Bhattacharya, 2009; Göktepe et al., 2010).

8.2. Conclusion

At an unprecedented temporal and spatial precision, optogenetic tools enable us to manipulate electrically active cells with light. This study documents our first attempts to model genetically engineered light-sensitive heart muscle cells, with the ultimate goal to control the cardiac system by mean of photostimulation. In contrast to electrical pacemakers, light delivery is minimally invasive, genetically targeted, and temporally precise. Most importantly, light can be delivered at a distance. Unlike pacing leads for electrical stimulation, which are known to have a high perforation risk, the light source for optical stimulation does not need to be in direct contact with the moving heart muscle. Light pacing might therefore be an attractive remote, less invasive, and more durable alternative to conventional electrical pacing. Unlike traditional electrical stimulation, optogenetic stimulation allows us to precisely control the selective permeability of the plasma membrane, its conductivity with respect to different ions, its sensitivity to light of different wavelengths, and the spatio-temporal evolution of different opening and closing profiles. Given this incredible freedom, there is a pressing need

to establish economic strategies to optimize the matrix of input variables. Predictive continuum models for photoelectrochemistry allow us to virtually probe landscapes of process parameters and identify optimal photostimulation sequences in various different tissues and organs. Discretized with finite element tools, they enable the combination of virtually any cell type on virtually any geometry. Our time-adaptive algorithm is highly efficient, conceptually modular, and easily portable to any commercial nonlinear finite element platform. While the photoelectrochemical behavior of living tissue is almost impossible to characterize *in vivo*, and little is known about the spatio-temporal distribution of sodium, potassium, and calcium ions, computational tools like ours allow us to predict action potential profiles and ionic concentrations across the heart *in silico* within the order of minutes. We believe that computational optogenetics will be widely applicable to predict the response of other genetically engineered, electrically active cells and, ultimately, support the design of novel therapies for various types of neuronal, musculoskeletal, pancreatic, and cardiac disorders such as depression, schizophrenia, cerebral palsy, paralysis, diabetes, pain syndromes, and cardiac arrhythmias.

Acknowledgments

This material was supported by the Biomedical Computation Graduate Training Grant 5T32GM063495-07 and the Stanford Graduate Fellowship to Jonathan Wong, by the California Institute for Regenerative Medicine Grant RC1-00151 and by the Stanford ARTS Fellowship to Oscar Abilez, and by the NSF CAREER Award CMMI-0952021 and the NIH Grant U54 GM072970 to Ellen Kuhl.

Appendix A

Our cardiac cell model is based on a well-characterized and frequently used ventricular cell model (ten Tusscher et al., 2004; Wong et al., 2011), enhanced by the channelrhodopsin photocurrent I_{Chr} and its corresponding gating variable g_{Chr2} . We characterize the cell through $n_{\text{ion}} = 4$ ion concentrations,

$$c_{\text{ion}} = [c_{\text{Na}}, c_{\text{K}}, c_{\text{Ca}}, c_{\text{Ca}}^{\text{sr}}] \quad (27)$$

where c_{Na} , c_{K} , and c_{Ca} are the intracellular sodium, potassium, and calcium concentrations, and $c_{\text{Ca}}^{\text{sr}}$ is the calcium concentration in the sarcoplasmic reticulum. Changes in these concentrations are brought about by an in- and outflux of ions which we describe through a total of $n_{\text{crt}} = 16$ ionic currents.

$$I_{\text{crt}} = [I_{\text{Na}}, I_{\text{bNa}}, I_{\text{NaK}}, I_{\text{NaCa}}, I_{\text{Chr2}}, I_{\text{K1}}, I_{\text{Kr}}, I_{\text{Ks}}, I_{\text{pK}}, I_{\text{t0}}, I_{\text{CaL}}, I_{\text{bCa}}, I_{\text{pCa}}, I_{\text{leak}}, I_{\text{up}}, I_{\text{rel}}] \quad (28)$$

These are the fast sodium current I_{Na} , the background sodium current I_{bNa} , the sodium potassium pump current I_{NaK} , the sodium calcium exchanger current I_{NaCa} , the channelrhodopsin photocurrent I_{Chr2} , the inward rectifier current I_{K1} , the rapid delayed rectifier current I_{Kr} , the slow delayed rectifier current I_{Ks} , the plateau potassium current I_{pK} , the transient outward current I_{t0} , the L-type calcium current I_{CaL} , the background calcium current I_{bCa} , the plateau calcium current I_{pCa} , the leakage current I_{leak} , and sarcoplasmic reticulum uptake and release currents I_{up} and I_{rel} . The activation and inactivation of these currents is governed by the transmembrane potential ϕ , and by $n_{\text{gate}} = 14$ gating variables:

$$g_{\text{gate}} = [g_{\text{m}}, g_{\text{h}}, g_{\text{j}}, g_{\text{Chr2}}, g_{\text{xr1}}, g_{\text{xr2}}, g_{\text{xs}}, g_{\text{r}}, g_{\text{s}}, g_{\text{d}}, g_{\text{f}}, g_{\text{K1}\infty}, g_{\text{fCa}}, g_{\text{g}}] \quad (29)$$

In particular, these are the sodium activation gate g_{m} , the fast and slow sodium inactivation gates g_{h} and g_{j} , the channelrhodopsin activation gate g_{Chr2} , the rapid delayed rectifier activation and inactivation gates g_{xr1} and g_{xr2} , the slow delayed rectifier activation gate g_{xs} , the transient potassium activation and inactivation gates g_{r} and g_{s} , the long-lasting L-type calcium channel activation and inactivation gates g_{d} , g_{f} , and g_{fCa} , and the calcium release activation gate g_{g} . We will now specify the mathematic model for the concentrations c_{ion} , currents I_{crt} , and gating variables g_{gate} . In Table 1, we summarize all model parameters, their physical interpretations, and their parameter values (ten Tusscher et al., 2004; Wong et al., 2011).

A.1. Sodium concentration, currents, and gating variables

Sodium plays a crucial role in generating the fast upstroke in the initial phase of the action potential. At rest, both electrical forces and chemical gradients pull extracellular sodium ions into the cell. The influx of sodium ions is small, however, since at rest, the membrane is relatively impermeable to sodium. An external stimulus above a critical threshold value, here generated through either photostimulation or through active neighboring cells, opens the fast sodium channels to initiate a rapid inflow of sodium ions associated with the rapid depolarization of the cell membrane. The transmembrane potential increases drastically by more than 100 mV in less than 2 ms, see Fig. 9. At the end of the upstroke, the cell membrane is positively charged, and the fast sodium channels return to their closed state. The sodium concentration

$$\dot{c}_{\text{Na}} = -\frac{C}{VF} [I_{\text{Na}} + I_{\text{bNa}} + 3I_{\text{NaK}} + 3I_{\text{NaCa}} + I_{\text{Chr2}}] \quad (30)$$

changes in response to the fast sodium current I_{Na} , the background sodium current I_{bNa} , the sodium potassium pump current I_{NaK} , and the sodium calcium exchanger current I_{NaCa} , scaled by the membrane capacitance per unit surface area

Table 1
Parameters of the proposed human cardiac muscle cell model. Symbols, physical interpretations, and parameter values.

R	Universal gas constant	$8.3143 \text{ J K}^{-1} \text{ mol}^{-1}$
T	Temperature	310 K
V	Cytoplasmic volume	$16,404 \mu\text{m}^3$
F	Faraday constant	$96,4867 \text{ C/mmol}$
C	Membrane capacitance	185 pF
V^{sr}	Volume of sarcoplasmic reticulum	$1094 \mu\text{m}^3$
C_{Na0}	Extracellular sodium concentration	140 mM
C_{K0}	Extracellular potassium concentration	5.4 mM
C_{Ca0}	Extracellular calcium concentration	2 mM
$I_{\text{NaK}}^{\text{max}}$	Maximum sodium potassium pump current	1.362 pA/pF
$I_{\text{NaCa}}^{\text{max}}$	Maximum sodium calcium exchanger current	1000 pA/pF
$I_{\text{leak}}^{\text{max}}$	Maximum leakage current	0.08 s^{-1}
$I_{\text{up}}^{\text{max}}$	Maximum sarcoplasmic reticulum calcium uptake current	0.425 mM/s
$I_{\text{rel}}^{\text{max}}$	Maximum sarcoplasmic reticulum calcium release current	8.232 mM/s
$C_{\text{Na}}^{\text{max}}$	Maximum fast sodium conductance	14.838 nS/pF
$C_{\text{bNa}}^{\text{max}}$	Maximum background sodium conductance	0.00029 nS/pF
$C_{\text{KI}}^{\text{max}}$	Maximum inward rectifier conductance	5.405 nS/pF
$C_{\text{Kr}}^{\text{max}}$	Maximum rapid delayed rectifier conductance	0.0096 nS/pF
$C_{\text{Ks,epi}}^{\text{max}}$	Maximum slow delayed rectifier conductance for epicardial cells	0.245 nS/pF
$C_{\text{Ks,endo}}^{\text{max}}$	Maximum slow delayed rectifier conductance for endocardial cells	0.245 nS/pF
$C_{\text{Ks,M}}^{\text{max}}$	Maximum slow delayed rectifier conductance for M cells	0.062 nS/pF
$C_{\text{pK}}^{\text{max}}$	Maximum potassium pump conductance	0.0146 nS/pF
$C_{\text{t0,epi}}^{\text{max}}$	Maximum transient outward conductance for epicardial cells	0.294 nS/pF
$C_{\text{t0,endo}}^{\text{max}}$	Maximum transient outward conductance for endocardial cells	0.073 nS/pF
$C_{\text{t0,M}}^{\text{max}}$	Maximum transient outward conductance for M cells	0.294 nS/pF
$C_{\text{CaI}}^{\text{max}}$	Maximum calcium conductance	$0.175 \text{ mm}^3/[\mu\text{Fs}]$
$C_{\text{bCa}}^{\text{max}}$	Maximum background calcium conductance	0.000592 nS/pF
$C_{\text{pCa}}^{\text{max}}$	Maximum plateau calcium conductance	0.825 nS/pF
C_{NaCa}	Half saturation sodium calcium exchanger concentration	87.50 mM
C_{CaNa}	Half saturation calcium sodium exchanger concentration	1.38 mM
C_{NaK}	Half saturation sodium potassium pump concentration	40.00 mM
C_{KNa}	Half saturation potassium sodium pump concentration	1.00 mM
C_{pCa}	Half saturation plateau calcium concentration	0.0005 mM
C_{up}	Half saturation sarcoplasmic reticulum calcium uptake	0.00025 mM
C_{rel}	Half saturation sarcoplasmic reticulum calcium release	0.25 mM
C_{buf}	Half saturation calcium buffer concentration	0.001 mM
C_{tot}	Total calcium buffer concentration	0.15 mM
$C_{\text{buf}}^{\text{sr}}$	Half saturation sarcoplasmic reticulum calcium buffer concentration	0.3 mM
$C_{\text{tot}}^{\text{sr}}$	Total sarcoplasmic reticulum calcium buffer concentration	10 mM
$k_{\text{NaCa}}^{\text{sat}}$	Sodium calcium saturation factor	0.1
p_{KNa}	Sodium permeability factor	0.03
γ_{rel}	Weighting factor	2.0
γ_{NaCa}	Pump current enhancing factor	2.5
γ	Sodium calcium factor	0.35

$C=185 \text{ pF}$, the cytoplasmic volume $V=16,404 \mu\text{m}^3$, and the Faraday constant $F=96.4867 \text{ C/mmol}$. The scaling factor three indicates that both the sodium potassium pump and the sodium calcium exchanger operate at a three-to-two ratio. The sodium related currents are defined as follows:

$$I_{\text{Na}} = C_{\text{Na}}^{\text{max}} g_m^3 g_h g_j [\phi - \phi_{\text{Na}}]$$

$$I_{\text{bNa}} = C_{\text{bNa}}^{\text{max}} [\phi - \phi_{\text{Na}}]$$

$$I_{\text{NaK}} = I_{\text{NaK}}^{\text{max}} [C_{\text{K0}} C_{\text{Na}}] [C_{\text{Na}} + C_{\text{NaK}}] [C_{\text{K0}} + C_{\text{KNa}}] [1 + 0.1245 e^{-0.1 \phi F / RT} + 0.0353 e^{-\phi F / RT}]^{-1}$$

$$I_{\text{NaCa}} = I_{\text{NaCa}}^{\text{max}} [e^{\gamma \phi F / RT} C_{\text{Na}}^3 C_{\text{Ca0}} - e^{(\gamma-1) \phi F / RT} C_{\text{Na0}}^3 C_{\text{Ca}} \gamma_{\text{NaCa}}] [C_{\text{NaCa}}^3 + C_{\text{Na0}}^3] [C_{\text{CaNa}} + C_{\text{Ca0}}] [1 + k_{\text{NaCa}}^{\text{sat}} e^{(\gamma-1) \phi F / RT}]^{-1}$$

$$I_{\text{Chr2}} = C_{\text{Chr2}} g_{\text{Chr2}} [\phi - \phi_{\text{Chr2}}]$$

where the scaling factors are the maximum fast sodium conductance $C_{\text{Na}}^{\text{max}} = 14.838$ nS/pF, the maximum background sodium conductance $C_{\text{bNa}}^{\text{max}} = 0.00029$ nS/pF, the maximum sodium potassium pump current $I_{\text{NaK}}^{\text{max}} = 1.362$ pA/pF, and the maximum sodium calcium exchanger current $I_{\text{NaCa}}^{\text{max}} = 1000$ pA/pF. The key player in generating the rapid upstroke is the fast sodium current I_{Na} . It follows a well-characterized three-gate formulation of Beeler and Reuter (1977) type in terms of the sodium activation gate g_{m} , the fast sodium inactivation gate g_{h} , and the slow sodium inactivation gate g_{j} . Classical Hodgkin–Huxley type equations, $\dot{g}_{\text{gate}} = [g_{\text{gate}}^{\infty} - g_{\text{gate}}]/\tau_{\text{gate}}$, define their evolution in terms of the steady state value g_{gate}^{∞} and the time constant associated with reaching the steady state τ_{gate} . For the sodium activation gate, $\dot{g}_{\text{m}} = [g_{\text{m}}^{\infty} - g_{\text{m}}]/\tau_{\text{m}}$, which initiates the rapid upstroke, they take the following explicit representations:

$$\begin{aligned} g_{\text{m}}^{\infty} &= [1 + e^{(-56.86 - \phi)/9.03}]^{-2} \\ \tau_{\text{m}} &= 0.1[1 + e^{(-60 - \phi)/5}]^{-1} [[1 + e^{(\phi + 35)/5}]^{-1} + [1 + e^{(\phi - 50)/200}]^{-1}] \end{aligned} \quad (32)$$

The kinetics of inactivation are exponential. For the fast sodium inactivation gate, $\dot{g}_{\text{h}} = [g_{\text{h}}^{\infty} - g_{\text{h}}]/\tau_{\text{h}}$, which initiates a fast inactivation of the sodium channel almost instantaneously after the rapid upstroke, we express the steady state value and the corresponding time constant as follows:

$$\begin{aligned} g_{\text{h}}^{\infty} &= [1 + e^{(\phi + 71.55)/7.43}]^{-2} \\ \tau_{\text{h}} &= \begin{cases} 0.1688[1 + e^{-(\phi + 10.66)/11.1}] & \text{if } \phi \geq -40 \\ [0.057e^{-(\phi + 80)/6.8} + 2.7e^{0.079\phi} + 3.1 \times 10^5 e^{0.3485\phi}]^{-1} & \text{if } \phi < -40 \end{cases} \end{aligned} \quad (33)$$

For the slow sodium inactivation gate, $\dot{g}_{\text{j}} = [g_{\text{j}}^{\infty} - g_{\text{j}}]/\tau_{\text{j}}$, which gradually inactivates the fast sodium channel over a time span of 100–200 ms, we express these constants in the following form:

$$\begin{aligned} g_{\text{j}}^{\infty} &= [1 + e^{(\phi + 71.55)/7.43}]^{-2} \\ \tau_{\text{j}} &= [\alpha_{\text{j}} + \beta_{\text{j}}]^{-1} \\ \alpha_{\text{j}} &= \begin{cases} 0 & \text{if } \phi \geq -40 \\ [-2.5428 \times 10^4 e^{0.2444\phi} - 6.948 \times 10^{-6} e^{-0.04391\phi}][\phi + 37.78][1 + e^{0.311(\phi + 79.23)}]^{-1} & \text{if } \phi < -40 \end{cases} \\ \beta_{\text{j}} &= \begin{cases} 0.6e^{0.057\phi}[1 + e^{-0.1(\phi + 32)}]^{-1} & \text{if } \phi \geq -40 \\ 0.02424e^{-0.01052\phi}[1 + e^{-0.1378(\phi + 40.14)}]^{-1} & \text{if } \phi < -40 \end{cases} \end{aligned} \quad (34)$$

The sodium potassium pump I_{NaK} , a metabolic pump that continuously expels sodium ions from the cell interior and pumps in potassium ions, is responsible to remove the sodium ions, which had entered the cell rapidly during the fast upstroke. The sodium calcium exchanger I_{NaCa} also affects the intracellular sodium concentration through the expulsion of intracellular calcium ions. The additional parameters that characterize the sodium potassium pump current I_{NaK} and for the sodium calcium exchanger current I_{NaCa} are the extracellular sodium, potassium, and calcium concentrations $c_{\text{Na0}} = 140$ mM, $c_{\text{K0}} = 5.4$ mM, and $c_{\text{Ca0}} = 2$ mM, the half saturation constants $c_{\text{CaNa}} = 1.38$ mM, $c_{\text{NaCa}} = 87.5$ mM, $c_{\text{KNa}} = 1$ mM, $c_{\text{NaK}} = 40$ mM, the sodium calcium saturation factor $k_{\text{NaCa}}^{\text{sat}} = 0.1$, the outward sodium calcium pump current enhancing factor $\gamma_{\text{NaCa}} = 2.5$, and the voltage dependent sodium calcium parameter $\gamma = 0.35$.

A.2. Potassium concentration, currents, and gating variables

Potassium plays an important role in maintaining the appropriate action potential profile in all four phases after the rapid upstroke. Unlike for sodium, the electrical force that pulls potassium ions inward is slightly weaker than the chemical force of diffusion pulling potassium ions outward. Accordingly, potassium tends to leave the resting cell. At the end of the rapid upstroke, before the beginning of the plateau, we can observe an early, brief period of limited repolarization governed by the voltage-activated transient outward current I_{t0} . During the following plateau phase, we observe an influx of calcium ions which is balanced by the efflux of an equal amount of positively charged potassium ions, mainly regulated by the rapid and slow delayed rectifier currents I_{Kr} and I_{Ks} . The final repolarization phase is almost exclusive caused to potassium ions leaving the cell such that the membrane potential can return to its resting state, see Fig. 9. In summary, four major currents control the evolution of the potassium concentration,

$$\dot{c}_{\text{K}} = -\frac{C}{VF} [I_{\text{K1}} + I_{\text{Kr}} + I_{\text{Ks}} - 2I_{\text{NaK}} + I_{\text{pK}} + I_{\text{t0}}] \quad (35)$$

the inward rectifier current I_{K1} , the rapid delayed rectifier current I_{Kr} , the slow delayed rectifier current I_{Ks} , and the transient outward current I_{t0} . The sodium potassium pump current I_{NaK} and the plateau potassium current I_{pK} play a minor role. The six potassium related currents scale by the membrane capacitance per unit surface area $C = 185$ pF, by

the cytoplasmic volume $V = 16,404 \mu\text{m}^3$, and by the Faraday constant $F = 96,4867 \text{ C/mmol}$. We adopt their following definitions:

$$\begin{aligned}
 I_{K1} &= C_{K1}^{\max} g_{K1}^{\infty} [c_{K0}/5.4]^{1/2} [\phi - \phi_K] \\
 I_{Kr} &= C_{Kr}^{\max} g_{xr1} g_{xr2} [c_{K0}/5.4]^{1/2} [\phi - \phi_K] \\
 I_{Ks} &= C_{Ks}^{\max} g_{xs}^2 [\phi - \phi_{Ks}] \\
 I_{NaK} &= I_{NaK}^{\max} [c_{K0} c_{Na}] [(c_{Na} + c_{NaK}) [c_{K0} + c_{KNa}] [1 + 0.1245 e^{-0.1\phi F/RT} + 0.0353 e^{-\phi F/RT}]]^{-1} \\
 I_{pK} &= C_{pK}^{\max} [1 + e^{(25-\phi)/5.98}]^{-1} [\phi - \phi_K] \\
 I_{t0} &= C_{t0}^{\max} g_r g_s [\phi - \phi_K]
 \end{aligned} \tag{36}$$

where the individual scaling factors are the maximum inward rectifier conductance $C_{K1}^{\max} = 5.405 \text{ nS/pF}$, the maximum rapid delayed rectifier conductance $C_{Kr}^{\max} = 0.096 \text{ nS/pF}$, the maximum slow delayed rectifier conductance for epicardial and endocardial cells $C_{Ks, \text{epi}}^{\max} = C_{Ks, \text{endo}}^{\max} = 0.245 \text{ nS/pF}$ and for M cells $C_{Ks, M}^{\max} = 0.062 \text{ nS/pF}$, the maximum sodium potassium pump current $I_{NaK}^{\max} = 1.362 \text{ pA/pF}$, the maximum potassium pump conductance $C_{pK}^{\max} = 0.0146 \text{ nS/pF}$, and the maximum transient outward conductance for epicardial and M cells $C_{t0, \text{epi}}^{\max} = C_{t0, M}^{\max} = 0.294 \text{ nS/pF}$ and for endocardial cells $C_{t0, \text{endo}}^{\max} = 0.073 \text{ nS/pF}$. The maximum inward rectifier current I_{K1} , which is most active during the later phases of the action potential, depends explicitly on the extracellular potassium concentration $c_{K0} = 5.4 \text{ mM}$. It scales with the time-independent inward rectification factor g_{K1}^{∞} parameterized in terms of the potential equilibrium potential ϕ_K :

$$g_{K1}^{\infty} = \alpha_{K1} [\alpha_{K1} + \beta_{K1}]^{-1} \quad \text{with} \quad \begin{aligned} \alpha_{K1} &= 0.1 [1 + e^{0.06(\phi - \phi_K - 200)}]^{-1} \\ \beta_{K1} &= [3e^{0.0002(\phi - \phi_K + 100)} + e^{0.1(\phi - \phi_K - 10)}] [1 + e^{-0.5(\phi - \phi_K)}]^{-1} \end{aligned} \tag{37}$$

A balanced influx of calcium ions and efflux of potassium ions governs the action potential plateau. In particular, the rapid and slow delayed rectifier currents I_{Kr} and I_{Ks} govern the potassium efflux. The channel for the rapid delayed rectifier current I_{Kr} is gated by an activation gate $\dot{g}_{x1} = [g_{x1}^{\infty} - g_{x1}]/\tau_{x1}$ with the steady state value and time constant given as

$$\begin{aligned}
 g_{xr1}^{\infty} &= [1 + e^{(-26-\phi)/7}]^{-1} \\
 \tau_{xr1} &= 2700 [1 + e^{(-45-\phi)/10}]^{-1} [1 + e^{(\phi+30)/11.5}]^{-1},
 \end{aligned} \tag{38}$$

and by an inactivation gate $\dot{g}_{x2} = [g_{x2}^{\infty} - g_{x2}]/\tau_{x2}$, with the following steady state value and time constant:

$$\begin{aligned}
 g_{xr2}^{\infty} &= [1 + e^{(\phi+88)/24}]^{-1} \\
 \tau_{xr2} &= 3.36 [1 + e^{(-60-\phi)/20}]^{-1} [1 + e^{(\phi-60)/20}]^{-1}
 \end{aligned} \tag{39}$$

The channel for the slow delayed rectifier current I_{Ks} is a function of the reversal potential $\phi_{Ks} = RT/F \log([c_{K0} + p_{KNa} c_{Na0}]/[c_K + p_{KNa} c_{Na}])^{-1}$ parameterized in terms of its permeability to sodium ions $p_{KNa} = 0.03$. It is gated by an activation gate $\dot{g}_{xs} = [g_{xs}^{\infty} - g_{xs}]/\tau_{xs}$ in terms of the following parameterization:

$$\begin{aligned}
 g_{xs}^{\infty} &= [1 + e^{(-5-\phi)/14}]^{-1} \\
 \tau_{xs} &= 1100 [1 + e^{(-10-\phi)/6}]^{-1/2} [1 + e^{(\phi-60)/20}]^{-1}
 \end{aligned} \tag{40}$$

The transient potassium outward current I_{t0} is responsible for the transition between the rapid upstroke and the plateau phase, where it generates an early short period of limited repolarization. It is gated by a voltage-dependent activation gate \dot{g}_r with $\dot{g}_r = [g_r^{\infty} - g_r]/\tau_r$ defined through the following steady state value and time constant:

$$\begin{aligned}
 g_r^{\infty} &= [1 + e^{(20-\phi)/6}]^{-1} \\
 \tau_r &= 9.5 e^{-(\phi+40)^2/1800} + 0.8
 \end{aligned} \tag{41}$$

and by the voltage-dependent inactivation gate \dot{g}_s with $\dot{g}_s = [g_s^{\infty} - g_s]/\tau_s$ with the steady state value and time constant given as follows:

$$\left. \begin{aligned} g_s^{\infty} &= [1 + e^{(\phi+20)/5}] \\ \tau_s &= 85 e^{-(\phi+45)^2/320} + 5 [1 + e^{(\phi-20)/5}] + 3 \end{aligned} \right\} \text{epicardium} \quad \left. \begin{aligned} g_s^{\infty} &= [1 + e^{(\phi+28)/5}] \\ \tau_s &= 1000 e^{-(\phi+67)^2/1000} + 8 \end{aligned} \right\} \text{endocardium} \tag{42}$$

This voltage dependent potassium inactivation gate displays a significantly different behavior for epicardial and endocardial cells and is therefore characterized differently in different regions of the heart. Similar to the previous subsection, we have introduced the extracellular sodium and potassium concentrations $c_{Na0} = 140 \text{ mM}$ and $c_{K0} = 5.4 \text{ mM}$, and the half saturation constants $c_{KNa} = 1 \text{ mM}$ and $c_{NaK} = 40 \text{ mM}$.

A.3. Calcium concentration, currents, and gating variables

Calcium is the key player to translate electrical excitation into mechanical contraction. During the plateau of the action potential, calcium ions enter the cell through calcium channels that typically activate and inactivate smoothly and more slowly than the fast sodium channels. The influx of positively charged calcium ions through the L-type calcium channel I_{CaL} is balanced by an efflux of positively charged potassium ions. The letter L indicates the long lasting nature of the inward calcium current. Overall, the intracellular calcium concentration evolves in response to seven currents,

$$\dot{c}_{Ca} = \gamma_{Ca} \left[-\frac{C}{2VF} [I_{CaL} + I_{bCa} + I_{pCa} - 2I_{NaCa}] + I_{leak} - I_{up} + I_{rel} \right] \quad (43)$$

the L-type calcium current I_{CaL} , the background calcium current I_{bCa} , the plateau calcium current I_{pCa} , and the sodium calcium pump current I_{NaCa} , weighted by the membrane capacitance per unit surface area $C = 185$ pF, the cytoplasmic volume $V = 16,404 \mu\text{m}^3$, and the Faraday constant $F = 96,4867$ C/mmol. In addition, the leakage current I_{leak} , the sarcoplasmic reticulum uptake current I_{up} , and the sarcoplasmic reticulum release current I_{rel} affect the intracellular calcium concentration through a calcium exchange with the sarcoplasmic reticulum. We adopt the following definitions for the individual calcium related currents,

$$\begin{aligned} I_{CaL} &= C_{CaL}^{\max} g_d g_f g_{fCa} [4\phi F^2 / [RT] [c_{Ca} e^{2\phi F / [RT]} - 0.341 c_{Ca0}] [e^{2\phi F / [RT]} - 1]^{-1} \\ I_{bCa} &= C_{bCa}^{\max} [\phi - \phi_{Ca}] \\ I_{pCa} &= C_{pCa}^{\max} c_{Ca} [c_{pCa} + c_{Ca}]^{-1} \\ I_{NaCa} &= I_{NaCa}^{\max} [e^{\gamma\phi F / RT} c_{Na}^3 c_{Ca0} - e^{(\gamma-1)\phi F / RT} c_{Na0}^3 c_{Ca} \gamma_{NaCa}] [(c_{NaCa}^3 + c_{Na0}^3) [c_{CaNa} + c_{Ca0}] [1 + K_{NaCa}^{\text{sat}} e^{(\gamma-1)\phi F / RT}]]^{-1} \\ I_{leak} &= I_{leak}^{\max} [c_{Ca}^{\text{sr}} - c_{Ca}] \\ I_{up} &= I_{up}^{\max} [1 + c_{up}^2 / c_{Ca}^2]^{-1} \\ I_{rel} &= I_{rel}^{\max} g_d g_g [1 + \gamma_{rel} c_{Ca}^{\text{sr}2} (c_{rel}^2 + c_{Ca}^{\text{sr}2})^{-1}] \end{aligned} \quad (44)$$

where the individual scaling factors are the maximum calcium conductance $C_{CaL}^{\max} = 0.175 \text{ mm}^3 \mu\text{F}^{-1} \text{ s}^{-1}$, the maximum background calcium conductance $C_{bCa}^{\max} = 0.000592 \text{ nS/pF}$, the maximum plateau calcium conductance $C_{pCa}^{\max} = 0.825 \text{ nS/pF}$, the maximum sodium calcium pump current $I_{NaCa}^{\max} = 1000 \text{ pA/pF}$, the maximum leakage current $I_{leak}^{\max} = 0.08 \text{ s}^{-1}$, the maximum sarcoplasmic reticulum calcium uptake current $I_{up}^{\max} = 0.000425 \text{ mM/ms}$, and the maximum sarcoplasmic reticulum calcium release current $I_{rel}^{\max} = 8.232 \text{ mM/s}$. The major calcium channel, the long-lasting L-type calcium channel I_{CaL} , opens and closes in response to the voltage-dependent activation gate $g_d = [g_d^{\infty} - g_d] / \tau_g$ characterized through the following steady state value and time constant:

$$\begin{aligned} g_d^{\infty} &= [1 + e^{(-5-\phi)/7.5}]^{-1} \\ \tau_d &= [1.4[1 + e^{(-35-\phi)/13}]^{-1} + 0.25][1.4[1 + e^{(\phi+5)/5}] + [1 + e^{(50-\phi)/20}]] \end{aligned} \quad (45)$$

in response to the voltage-dependent inactivate gate $g_f = [g_f^{\infty} - g_f] / \tau_f$ characterized through

$$\begin{aligned} g_f^{\infty} &= [1 + e^{(\phi+20)/7}]^{-1} \\ \tau_f &= 1125 e^{-(\phi+27)^2/240} + 165 [1 + e^{(25-\phi)/10}]^{-1} + 80 \end{aligned} \quad (46)$$

and in response to the intracellular calcium dependent inactivation gate $g_{fCa} = [g_{fCa}^{\infty} - g_{fCa}] / \tau_{fCa}$ characterized through

$$\begin{aligned} g_{fCa}^{\infty} &= 0.685 [1 + (c_{Ca} / 0.000325)^8]^{-1} + 0.1 [1 + e^{(c_{Ca} - 0.0005) / 0.0001}]^{-1} + 0.2 [1 + e^{(c_{Ca} - 0.00075) / 0.0008}]^{-1} + 0.23] \\ \tau_{fCa} &= \begin{cases} \infty & \text{if } g_{fCa}^{\infty} > g_{fCa} \text{ and } \phi \geq -60 \text{ mV} \\ 2 \text{ ms} & \text{otherwise} \end{cases} \end{aligned} \quad (47)$$

Accordingly, the steady state response g_{fCa}^{∞} has a switch-like shape when going from no inactivation to considerable but incomplete inactivation, depending mildly on the calcium concentration c_{Ca} for suprathreshold concentrations. Last, the calcium-induced calcium release current I_{rel} is characterized through the activation gate g_d , the same gate that is also

activating the L-type calcium channel of I_{CaL} , and through the calcium-dependent inactivation gate $\dot{g}_g = [g_g^\infty - g_g]/\tau_g$ characterized through the following steady state value and time constant:

$$g_g^\infty = \begin{cases} [1 + c_{Ca}^6/0.00035^6]^{-1} & \text{if } c_{Ca} \leq 0.00035 \\ [1 + c_{Ca}^{16}/0.00035^{16}]^{-1} & \text{otherwise} \end{cases}$$

$$\tau_g = \begin{cases} \infty & \text{if } g_g^\infty > g_g \text{ and } \phi \geq -60 \text{ mV} \\ 2 \text{ ms} & \text{otherwise} \end{cases} \quad (48)$$

The remaining parameters governing the response of the plateau calcium current I_{pCa} , the calcium uptake current I_{up} , and the sarcoplasmic reticulum calcium release current I_{rel} are the half saturation constants for the plateau calcium concentration $c_{pCa} = 0.0005$ mM, for the sarcoplasmic reticulum calcium uptake $c_{up} = 0.00025$ mM, and for the sarcoplasmic reticulum calcium release $c_{rel} = 0.25$ mM, respectively. The parameter $\gamma_{NaCa} = 2.5$ enhances the outward nature of the sodium calcium pump current I_{NaCa} . The additional parameter $\gamma_{rel} = 2$ weighs the relative influence of the sarcoplasmic reticulum calcium concentration on sarcoplasmic reticulum calcium release I_{rel} . Finally, we represent the total intracellular calcium concentration $c_{Ca}^{tot} = c_{Ca} + c_{Ca}^{buf}$ in the cytoplasm as the sum of the free intracellular calcium concentration c_{Ca} and the buffered calcium concentration $c_{Ca}^{buf} = [c_{Ca} c_{Ca}^{tot} / c_{Ca}^{buf}] [c_{Ca} - c_{Ca}^{buf}]^{-1}$. Accordingly, we scale the definition of the free intracellular calcium concentration in Eq. (43) with the parameter $\gamma_{Ca} = [1 + [c_{tot} c_{buf}] [c_{Ca} + c_{buf}]^{-2}]^{-1}$, where $c_{tot} = 0.15$ mM and $c_{buf} = 0.001$ mM are the total and half saturation cytoplasmic calcium buffer concentrations.

A.4. Sarcoplasmic reticulum calcium concentration, currents, and gating variables

The specification of the sarcoplasmic reticulum calcium concentration

$$\dot{c}_{Ca}^{sr} = \gamma_{Ca}^{sr} \frac{V}{V^{sr}} [-I_{leak} + I_{up} - I_{rel}] \quad (49)$$

is now relatively straightforward since it mimics the corresponding loss of intracellular calcium scaled by the ratio between the volume of the cytoplasm $V = 16,404 \mu\text{m}^3$ and the volume of the sarcoplasmic reticulum $V^{sr} = 1094 \mu\text{m}^3$. The leakage current I_{leak} , the sarcoplasmic reticulum uptake current I_{up} , and the sarcoplasmic reticulum release current I_{rel} are defined as before:

$$I_{leak} = I_{leak}^{max} [c_{Ca}^{sr} - c_{Ca}]$$

$$I_{up} = I_{up}^{max} [1 + c_{up}^2 / c_{Ca}^2]^{-1}$$

$$I_{rel} = I_{rel}^{max} g_d g_g [1 + \gamma_{rel} c_{Ca}^{sr 2} [c_{rel}^2 + c_{Ca}^{sr 2}]^{-1}] \quad (50)$$

We have already introduced the maximum leakage current $I_{leak}^{max} = 0.08 \text{ s}^{-1}$, the maximum sarcoplasmic reticulum calcium uptake current $I_{up}^{max} = 0.000425 \text{ mM/ms}$, and the maximum sarcoplasmic reticulum calcium release current $I_{rel}^{max} = 8.232 \text{ mM/s}$, the half saturation constants for the calcium uptake $c_{up} = 0.00025$ mM, and for the calcium release $c_{rel} = 0.25$ mM, and the weighting coefficient $\gamma_{rel} = 2$ in the previous subsection. Finally, we introduce the total calcium concentration in the sarcoplasmic reticulum $c_{Ca}^{sr tot} = c_{Ca}^{sr} + c_{Ca}^{sr buf}$ as the sum of the free sarcoplasmic reticulum calcium concentration c_{Ca}^{sr} and the buffered sarcoplasmic reticulum calcium concentration $c_{Ca}^{sr buf} = [c_{Ca}^{sr} c_{Ca}^{sr tot} / c_{Ca}^{sr buf}] [c_{Ca}^{sr} - c_{Ca}^{sr buf}]^{-1}$. Accordingly, we scale the free sarcoplasmic reticulum calcium concentration in Eq. (49) by the parameter $\gamma_{Ca}^{sr} = [1 + [c_{tot}^{sr} c_{buf}^{sr}] [c_{Ca}^{sr} + c_{buf}^{sr}]^{-2}]^{-1}$, where $c_{tot}^{sr} = 10$ mM and $c_{buf}^{sr} = 0.3$ mM are the total and half saturation sarcoplasmic reticulum calcium buffer concentrations.

References

- Abilez, O.J., Wong, J., Prakash, R., Deisseroth, K., Zarins, C.K., Kuhl, E., 2011. Multiscale computational models for optogenetic control of cardiac function. *Biophys. J.* 101, 1326–1334.
- Arrenberg, A.B., Stainier, D.Y.R., Baier, H., Huisken, J., 2010. Optogenetic control of cardiac function. *Science* 330, 971–974.
- Beeler, G.W., Reuter, H., 1977. Reconstruction of the action potential of ventricular myocardial fibers. *J. Physiol.* 268, 177–210.
- Berne, R.M., Levy, M.N. 2001. *Cardiovascular Physiology*, The Mosby Monograph Series.
- Boyden, E.S., Zhang, F., Bamberg, E., Nagel, G., Deisseroth, K., 2005. Millisecond-timescale, genetically targeted optical control of neural activity. *Nat. Neurosci.* 8, 1263–1268.
- Bruegmann, T., Malan, D., Hesse, M., Beiert, T., Fueggemann, C.J., Fleischmann, B.K., Sasse, P., 2010. Optogenetic control of heart muscle in vitro and in vivo. *Nat. Methods* 7, 897–900.
- Chen, M.Q., Wong, J., Kuhl, E., Giovannardi, L.B., Kovacs, G.T.A., 2011. Characterization of electrophysiological conduction in cardiomyocyte co-cultures using co-occurrence analysis. *Comput. Methods Biomech. Biomed. Eng.*, doi:10.1080/10255842.2011.615310.
- Criscione, J.C., McCulloch, A.D., Hunter, W.C., 2002. Constitutive framework optimized for myocardium and other high-strain, laminar materials with one fiber family. *J. Mech. Phys. Solids* 50, 1681–1702.
- Dal, H., Göktepe, S., Kaliske, M., Kuhl, E., 2011. A fully implicit finite element method for bidomain models of cardiac electrophysiology. *Comput. Methods Biomech. Biomed. Eng.*, doi:10.1080/10255842.2011.554410.
- Deisseroth, K., 2011. Optogenetics. *Nat. Methods* 8, 26–29.

- Dubin, D., 2000. Rapid Interpretation of EKGs. Cover Publishing Co, Fort Myers.
- Feng, F., Klug, W.S., 2006. Finite element modeling of lipid bilayer membranes. *J. Comput. Phys.* 220, 394–408.
- Furman, S., Schwedel, J.B., 1959. An intracardiac pacemaker for Stokes–Adams seizures. *New Engl. J. Med.* 261, 943–948.
- Givli, S., Bhattacharya, K., 2009. A coarse-grained model of the myofibril: overall dynamics and the evolution of non-uniformities. *J. Mech. Phys. Solids* 57, 221–243.
- Göktepe, S., Kuhl, E., 2009. Computational modeling of electrophysiology: a novel finite element approach. *Int. J. Numer. Methods Eng.* 79, 156–178.
- Göktepe, S., Wong, J., Kuhl, E., 2010. Atrial and ventricular fibrillation—computational simulation of spiral waves in cardiac tissue. *Arch. Appl. Mech.* 80, 569–580.
- Göktepe, S., Kuhl, E., 2010. Electromechanics of the heart—a unified approach to the strongly coupled excitation–contraction problem. *Comput. Mech.* 45, 227–243.
- Göktepe, S., Abilez, O.J., Kuhl, E., 2010. A generic approach towards finite growth with examples of athlete's heart, cardiac dilation, and cardiac wall thickening. *J. Mech. Phys. Solids* 58, 1661–1680.
- Hegemann, P., Gärtner, W., Uhl, R., 1991. All-trans retinal constitutes the functional chromophore in *Chlamydomonas* rhodopsin. *Biophys. J.* 60, 1477–1489.
- Hegemann, P., Ehlenbeck, S., Gradmann, D., 2005. Multiple photocycles of channelrhodopsin. *Biophys. J.* 89, 3911–3918.
- Hegemann, P., Möglich, A., 2011. Channelrhodopsin engineering and exploration of new optogenetic tools. *Nat. Methods* 8, 39–42.
- Ishizuka, T., Kakuda, M., Araki, R., Yawo, H., 2006. Kinetic evaluation of photosensitivity in genetically engineered neurons expressing green algae light-gated channels. *Neurosci. Res.* 54, 85–94.
- James, T.N., 1961. Morphology of the human atrioventricular node, with remarks pertinent to its electrophysiology. *Am. Heart J.* 62, 756–770.
- Jia, Z., Valiunas, V., Lu, Z., Bien, H., Liu, H., Wang, H.Z., Rosati, B., Brink, P.R., Cohen, I.S., Entcheva, E., 2011. Stimulating cardiac muscle by light: cardiac optogenetics by cell delivery. *Circ. Arrhythm. Electrophys.* 4, 753–760.
- Keener, J., Sneyd, J., 2004. *Mathematical Physiology*. Springer Science and Business Media.
- Khan, M.N., Joseph, G., Khaykin, Y., Ziada, K.M., Wilkoff, B.L., 2005. Delayed lead perforation: a disturbing trend. *Pacing Clin. Electrophys.* 28, 251–253.
- Kotikanyadanam, M., Göktepe, S., Kuhl, E., 2010. Computational modeling of electrocardiograms—a finite element approach towards cardiac excitation. *Int. J. Numer. Methods Biomed. Eng.* 26, 524–533.
- Mahapatra, S., Bybee, K.A., Bunch, J., Espinosa, R.E., Sinak, L.J., McGoan, M.D., Hayes, D.L., 2005. Incidence and predictors of cardiac perforation after permanent pacemaker placement. *Heart Rhythm* 2, 907–911.
- Matsuno-Yagi, A., Mukohata, Y., 1977. Two possible roles of bacteriorhodopsin; a comparative study of strains of *Halobacterium halobium* differing in pigmentation. *Biochem. Biophys. Res. Commun.* 78, 237–243.
- Modi, S., Krahn, A., Yee, R., 2011. Current concepts in pacing 2010–2011: the right and wrong way to pace. *Curr. Treat. Opt. Cardiovasc. Med.* 13, 370–384.
- Nagel, G., Ollig, D., Fuhrmann, M., Kateriya, S., Musti, A.M., Bamberg, E., Hegemann, P., 2002. Channelrhodopsin-1, a light-gated proton channel in green algae. *Science* 296, 2395–2398.
- Nagel, G., Szellas, T., Huhn, W., Kateriya, S., Adeishvili, N., Berthold, P., Ollig, D., Hegemann, P., Bamberg, E., 2003. Channelrhodopsin-2, a directly light-gated cation-selective membrane channel. *Proc. Natl. Acad. Sci.* 100, 13940–13945.
- Nikolic, K., Degenaar, P., Toumazou, C., 2006. Modeling and engineering aspects of Channelrhodopsin2 system for neural photostimulation. In: *Proceedings of the 28th IEEE EMBS*, vol. 40, pp. 1626–1629.
- Nikolic, K., Grossman, N., Grubb, M.S., Burrone, J., Toumazou, C., Degenaar, P., 2009. Photocycles of Channelrhodopsin-2. *Photochem. Photobiol.* 85, 400–411.
- Oesterhelt, D., Stoerkenius, W., 1971. Rhodopsin-like protein from the purple membrane of *Halobacterium halobium*. *Nat. New Biol.* 233, 149–152.
- Puwal, S., Roth, B.J., 2009. Optimization of feedback pacing for defibrillation. *IEEE Trans. Biomed. Eng.* 56, 532–534.
- Rausch, M.K., Dam, A., Göktepe, S., Abilez, O.J., Kuhl, E., 2011. Computational modeling of growth: systemic and pulmonary hypertension in the heart. *Biomech. Mod. Mechanobiol.* 10, 799–811.
- Reeves, D., Ursell, T., Sens, P., Kondev, J., Phillips, R., 2008. Membrane mechanics as a probe of ion-channel gating mechanisms. *Phys. Rev. E* 78, 041901-1–041901-11.
- Rush, S., Larsen, H., 1978. Practical algorithm for solving dynamic membrane equations. *IEEE Trans. Biomed. Eng.* 25, 389–392.
- Szobota, S., Isacoff, E.Y., 2010. Optical control of neuronal activity. *Ann. Rev. Biophys.* 39, 329–348.
- Taylor, R.L., 2011. FEAP—A Finite Element Analysis Program. Version 8.3, User Manual, University of California at Berkeley.
- Tsamis, A., Bothe, W., Kvitting, J.P., Swanson, J.C., Miller, D.C., Kuhl, E., 2011. Active contraction of cardiac muscle: in vivo characterization of mechanical activation sequences in the beating heart. *J. Mech. Behav. Biomed. Mater.* 4, 1167–1176.
- ten Tusscher, K.H.W.J., Noble, D., Noble, P.J., Panfilov, A.V., 2004. A model for human ventricular cardiomyocytes. *Am. J. Physiol. Heart Circ. Physiol.* 286, H1573–H1589.
- Ursell, T., Huang, K.C., Peterson, E., Phillips, R., 2007. Cooperative gating and spatial organization of membrane proteins through elastic interactions. *PLOS Comput. Biol.* 3, 803–812.
- Vsedolodov, N.N., 1998. *Biomolecular Electronics. An Introduction via Photosensitive Proteins*. Birkhauser, Boston.
- Wenk, J.F., Eslami, P., Zhang, Z., Xu, C., Kuhl, E., Gorman, J.H., Robb, J.D., Ratcliffe, M.B., Gorman, R.C., Guccione, J.M., 2011. A novel method for quantifying the in-vivo mechanical effect of material injected into a myocardial infarction. *Ann. Thorac. Surg.* 92, 935–941.
- Wong, J., Göktepe, S., Kuhl, E., 2011. Computational modeling of electrochemical coupling: a novel finite element approach towards ionic models for cardiac electrophysiology. *Comput. Methods Appl. Mech. Eng.* 200, 3139–3158.